Hydrol. Earth Syst. Sci., 29, 215–244, 2025
https://doi.org/10.5194/hess-29-215-2025

Hydrology and Earth System Sciences
Open Access
EGU

Quantifying the potential of using Soil Moisture Active Passive (SMAP) soil moisture variability to predict subsurface water dynamics

Aruna Kumar Nayak[1], **Xiaoyong Xu**[1,2], **Steven K. Frey**[3,4], **Omar Khader**[3,5], **Andre R. Erler**[3], **David R. Lapen**[6], **Hazen A. J. Russell**[7], **and Edward A. Sudicky**[3,4]

[1]Department of Chemical and Physical Sciences, University of Toronto Mississauga, Mississauga, ON, Canada
[2]Department of Geography, Geomatics and Environment, University of Toronto Mississauga, Mississauga, ON, Canada
[3]Aquanty, Waterloo, ON, Canada
[4]Department of Earth and Environmental Sciences, University of Waterloo, Waterloo, ON, Canada
[5]Department of Water and Water Structural Engineering, Zagazig University, Al Sharqia, Egypt
[6]Agriculture and Agri-Food Canada, Ottawa Research and Development Centre, Ottawa, ON, Canada
[7]Natural Resources Canada, Ottawa, ON, Canada

Correspondence: Xiaoyong Xu (xiaoyong.xu@utoronto.ca)

Received: 29 December 2023 – Discussion started: 15 January 2024
Revised: 28 October 2024 – Accepted: 19 November 2024 – Published: 15 January 2025

Abstract. Advances in satellite Earth observation have opened up new opportunities for global monitoring of soil moisture (SM) at fine to medium resolution, but satellite remote sensing can only measure the near-surface soil moisture (SSM). As such, it is critically important to examine the potential of satellite SSM measurements to derive the water resource variations in deeper subsurface. This study compares the SSM variability captured by the Soil Moisture Active and Passive (SMAP) satellite and the Soil Water Index (SWI) derived from SMAP SSM with subsurface SM and groundwater (GW) dynamics simulated by a high-resolution fully integrated surface water–groundwater model over an agriculturally dominated watershed in eastern Canada across two spatial scales, namely SMAP product grid (9 km) and watershed ($\sim 4000\,km^2$). SMAP measurements compare well with the hydrologic simulations in terms of SSM variability at both scales. Simulated subsurface SM and GW storage show lagged and smoother characteristics relative to SMAP SSM variability with an optimal delay of ~ 1 d for the 25–50 cm SM, ~ 6 d for the 50–100 cm SM, and ~ 11 d for the GW storage for both scales. Modeled subsurface SM dynamics agree well with the SWI derived from SMAP SSM using the classic characteristic time lengths (15 d for the 0–25 cm layer and 20 d for the 0–100 cm layer). The simulated GW storage showed a slightly delayed variation relative to the derived SWI. The quantified optimal characteristic time length T_{opt} for SWI estimation (by matching the variations in SMAP-derived SWI and modeled root zone SM) is comparable to T_{opt} obtained in other agricultural regions around the world. This work demonstrates SMAP SM measurements as a potentially useful aid when predicting root zone SM and GW dynamics and validating fully integrated hydrologic models across different spatial scales. This study also provides insights into the dynamics of near-surface–subsurface water interaction and the capabilities and approaches of satellite-based SM monitoring and high-resolution fully integrated hydrologic modeling.

1 Introduction

Accurate information on soil moisture (SM) and groundwater (GW) storage is essential for assessing water resources and making informed decisions for effective water resource management. SM can be monitored and measured using ground-based in situ sensor networks and remote sensing methods (e.g., Dobriyal et al., 2012). The in situ SM monitoring networks are able to provide continuous measure-

ments for different soil depths or profiles; however, the monitoring sites are typically sparse, especially at continental or global scales, causing difficulty in large-scale spatially distributed SM estimation (e.g., Jonard et al., 2018; Singh et al., 2019). Advances in satellite Earth observation have opened up opportunities for the large-scale and global monitoring of SM at fine to medium resolution (e.g., Bartalis et al., 2007; Entekhabi et al., 2010; Kerr et al., 2010; Njoku et al., 2003; Owe et al., 2008; Xu et al., 2014), but satellite remote sensing only measures the near-surface soil layer (the topmost few centimeters) and cannot directly observe the deeper soils. Further, NASA's Gravity Recovery and Climate Experiment (GRACE) and GRACE-Follow On (GRACE-FO) have made it possible to track changes in terrestrial water storage (TWS) by detecting Earth's gravitational changes (Tapley et al., 2004). The TWS observations, in combination with model outputs or reanalysis products, can be used to quantify GW storage dynamics (Famiglietti et al., 2011; Rodell et al., 2007, 2009, 2018; Syed et al., 2008; Thomas and Famiglietti, 2019; Zhu et al., 2022). However, the coarse-scale (a native resolution of $\sim 3^\circ$ in both latitude and longitude) monthly TWS changes provided by the GRACE/GRACE-FO observations cannot fully meet the needs for monitoring the variations in GW across different temporal and spatial scales.

As such, the potential of satellite near-surface soil moisture (SSM) measurements for estimating or predicting the variations in root zone SM and GW has received considerable attention over the past decades (e.g., Bouaziz et al., 2020; Ceballos et al., 2005; Ford et al., 2014; Nayak et al., 2021; Paulik et al., 2014; Sutanudjaja et al., 2013; Tian et al., 2020; Wagner et al., 1999; Zhao et al., 2008). One of the key steps for this important application is identification of the coupling strength and the associated temporal differences in response to wetting–drying processes among different subsurface layers, which can vary remarkably across different regions and different time windows depending on a suite of factors, such as depths considered, soil hydraulic properties, soil texture, climate conditions, and land cover (e.g., Albergel et al., 2008; Bouaziz et al., 2020; Wang et al., 2017).

The differences in responses to wetting–drying processes in the soil profile can be examined using in situ measurements (e.g., Mahmood et al., 2012; Wu et al., 2002) or hydrological models (e.g., Mahmood and Hubbard, 2007). The time-lagged cross-correlation in SM variations identified between the surface and deeper soil layers (e.g., Mahmood and Hubbard, 2007; Mahmood et al., 2012; Wu et al., 2002) may indicate that the deeper subsurface SM variability could be approximated by delaying the temporal variations in SSM. On the other hand, the deeper subsurface soil water content can be estimated by smoothing the SSM time series since soil water in the deeper layers typically exhibit smaller variations and longer response times to critical precipitation and drying events that occur at the surface (e.g., Albergel et al., 2008; Manfreda et al., 2014; Ragab, 1995; Wagner et al., 1999). A widely used smoothing method is the Soil Water Index (SWI) that estimates the subsurface SM profiles from the SSM time series using an exponential filter with the characteristic time length T as the only control parameter (Wagner et al., 1999). The optimal characteristic time length (T_{opt}) can be obtained by matching the SWI to reference root zone SM (e.g., Bouaziz et al., 2020; Ceballos et al., 2005; Ford et al., 2014; Paulik et al., 2014; Tian et al., 2020; Wagner et al., 1999).

Over the past decades, land surface and hydrological models have played an important role in quantifying T_{opt} for SWI estimation. Albergel et al. (2008) investigated the effects of various factors on T_{opt} for SWI estimation by a combined use of in situ and model data for soils in France. Wang et al. (2017) demonstrated the capability of vadose zone model simulations in quantifying the relationships between T_{opt} and its various influencing factors (precipitation, land cover, and soil hydraulic properties) over the continental United States. Bouaziz et al. (2020) utilized the root zone SM simulated by a process-based lumped hydrological model as reference to quantify T_{opt} values for SWI estimation from different satellite SM products across a number of watersheds in France. In addition, the inter-comparisons between satellite SM and modeled SM data have been central to intensive research efforts (e.g., Al-Yaari et al., 2014; Dorigo et al., 2010; Draper et al., 2013; Parrens et al., 2012).

Recent advances in high-resolution fully integrated surface water–groundwater modeling for Canadian basins (Erler et al., 2019; Frey et al., 2021; Xu et al., 2021; Aziz et al., 2023) have provided new opportunities for simulating water dynamics in the variably saturated subsurface domain. Such models present a better ability to reproduce realistic root zone SM and GW dynamics than surface water models used in previous studies. Hence, these models are well suited to help expand our understanding of connections between satellite SM and the variably saturated subsurface flow regime. Accordingly, this study aims to advance our understanding of (i) the coupling and response time differences between satellite SM dynamics and transient soil water and groundwater storage characteristics, (ii) the dependence of coupling and response time differences on spatial scale, (iii) the ability of state-of-the-art satellite SM monitoring to predict root zone SM and GW dynamics, and (iv) the ability of satellite SM data to assist with validation of large-scale integrated hydrologic models. To this end, the study herein examines the linkages between the Soil Moisture Active Passive (SMAP) SM, which represents one of the state-of-the-art satellite-based SM products, and the subsurface SM and GW dynamics simulated by a high-resolution fully integrated surface water–groundwater model of an agriculture-dominated watershed across two spatial scales, namely SMAP 9 km grid cell and watershed.

2 Data and methods

2.1 Study watershed

The study domain is the South Nation Watershed (SNW) in eastern Ontario, Canada (Fig. 1a). The SNW is an agriculture-dominated, mixed-use watershed with an areal coverage of about 3900 km^2 (Fig. 1b).

The major crop types grown in the area are corn and soybeans. In the agricultural fields, natural soil water drainage is typically slow on account of extensive clay loam soil (Fig. 1c). The agricultural region generally has low topographic relief (Fig. 1d), with artificial subsurface drainage (tile drains) to drain excess water from fields to facilitate crop productivity (Fig. 1e). The tile drains tend to be spaced about 15 to 17 m apart (Sunohara et al., 2015), with a total tile-drained area of 956 km^2 (about 25 % of the watershed). The watershed is characterized as having a humid temperate climate, a 20-year (1998–2017) average annual precipitation of about 1000 mm, and an average annual evapotranspiration of about 600 mm. The average water table is 1 to 3 m below surface across much of the agricultural landscape.

2.2 Satellite SSM and SWI

For this study, satellite-based SM retrievals are taken from the SMAP-enhanced L3 radiometer 9 km EASE-Grid SM (SPL3SMP_E) version 5 product (O'Neill et al., 2021). The SPL3SMP_E product provides daily composite estimates of near-surface ($\sim$ top 5 cm) SM at a resolution of 9 km, retrieved from the AM (descending half orbits) and PM (ascending half orbits) brightness temperatures observed by the SMAP radiometer. In this study, only the SPL3SMP_E AM retrievals are used since the AM product is superior to the PM product over the study region, which is consistent with the AM–PM product comparison over the Great Lakes region (Xu, 2020). The location of the SPL3SMP_E product 9 km grid cells over the SNW is illustrated in Fig. 1b. A filtering step (using the SMAP product's ancillary information) was conducted to remove the SMAP SM estimates that were affected by various adverse factors (e.g., open water, frozen surfaces, snow, rain, or radio frequency interference). This study uses the SMAP SM data between 31 March 2015 (the date when SMAP started operation) and 31 December 2017, which is the time span overlapping with the temporal coverage of model simulations used in this work (Sect. 2.3).

The SMAP SSM can be used to derive the moisture content in the deeper layers or entire unsaturated root zone with the SWI approach, which estimates the subsurface SM as a function of SSM utilizing an exponential filter (Wagner et al., 1999). The SWI method considers a near-surface soil layer and a subsurface layer. A water-balance approach is then applied to the two soil layers to compute the water fluxes across them, which are assumed to be proportional to their SM differences. In this study, we use the recursive exponential filter (Albergel et al., 2008), which is suitable for SWI estimation from the SSM observed at irregular time intervals. The SWI at time t_i is given by Eq. (1):

$$\mathrm{SWI}(t_i) = \mathrm{SWI}(t_{i-1}) + K(t_i)\,(\mathrm{SSM}(t_i) - \mathrm{SWI}(t_{i-1})), \quad (1)$$

where $\mathrm{SWI}(t_i)$ and $\mathrm{SWI}(t_{i-1})$ denote the SWI values at time t_i and t_{i-1}, respectively; $\mathrm{SSM}(t_i)$ represents the SMAP near-surface soil moisture at time t_i; and $K(t_i)$ is the gain at time t_i, which is given in a recursive form as in Eq. (2):

$$K(t_i) = \frac{K(t_{i-1})}{K(t_{i-1}) + \exp\left(\frac{-(t_i - t_{i-1})}{T}\right)}, \quad (2)$$

where $K(t_{i-1})$ is the gain at time t_{i-1}. The gain K ranges from 0 to 1 with the initialization $K(t_0) = 1$, while SWI is initialized using the SSM series, i.e., $\mathrm{SWI}(t_0) = \mathrm{SSM}(t_0)$. The parameter T is the characteristic time length in days and can be considered a surrogate for many factors (e.g., soil depth, soil properties, evaporation, and runoff) that can influence SM changes due to drying and wetting processes (Albergel et al., 2008; Wagner et al., 1999).

2.3 Fully integrated surface water–groundwater model

The high-resolution fully integrated surface water–groundwater simulations are conducted using HydroGeoSphere (HGS) (Aquanty, 2022; Hwang et al., 2014; Frey et al., 2021). HGS uses the one-dimensional (1D) Manning's open channel flow equation to govern river/stream flow, the diffusion wave equation to govern two-dimensional (2D) overland flow, and Richards' equation to govern three-dimensional (3D) variably saturated subsurface flow. The channel, surface, and subsurface regimes naturally interact with each other through the exchange of water fluxes in response to varying pressure gradients. Unlike loosely or sequentially coupled groundwater–surface water models, HGS is a fully integrated model, providing the simultaneous solution of the channel, surface, and subsurface flow regimes at each time step. Detailed information on HGS can be found in the relevant documents (Aquanty, 2022; Hwang et al., 2014; Frey et al., 2021).

Within the model there are seven subsurface layers that are composed of 3D triangular prisms, formed by superimposing eight mesh layers of planar elements from the soil surface downward to a depth of $\sim$ 35 m. In total, there are 171 609 planar elements per mesh layer, equating to a total 1 201 263 3D elements across the seven-layer subsurface domain. The 3D unstructured finite-element mesh that underpins the HGS model carries 125 m spatial resolution along Strahler 2+ streams and rivers and up to 375 m resolution in areas distal to the resolved surface water features. The 2D overland flow domain (composed of planar elements) and the 1D channel domain (composed of linear elements) are both superimposed onto the subsurface 3D domain. In the

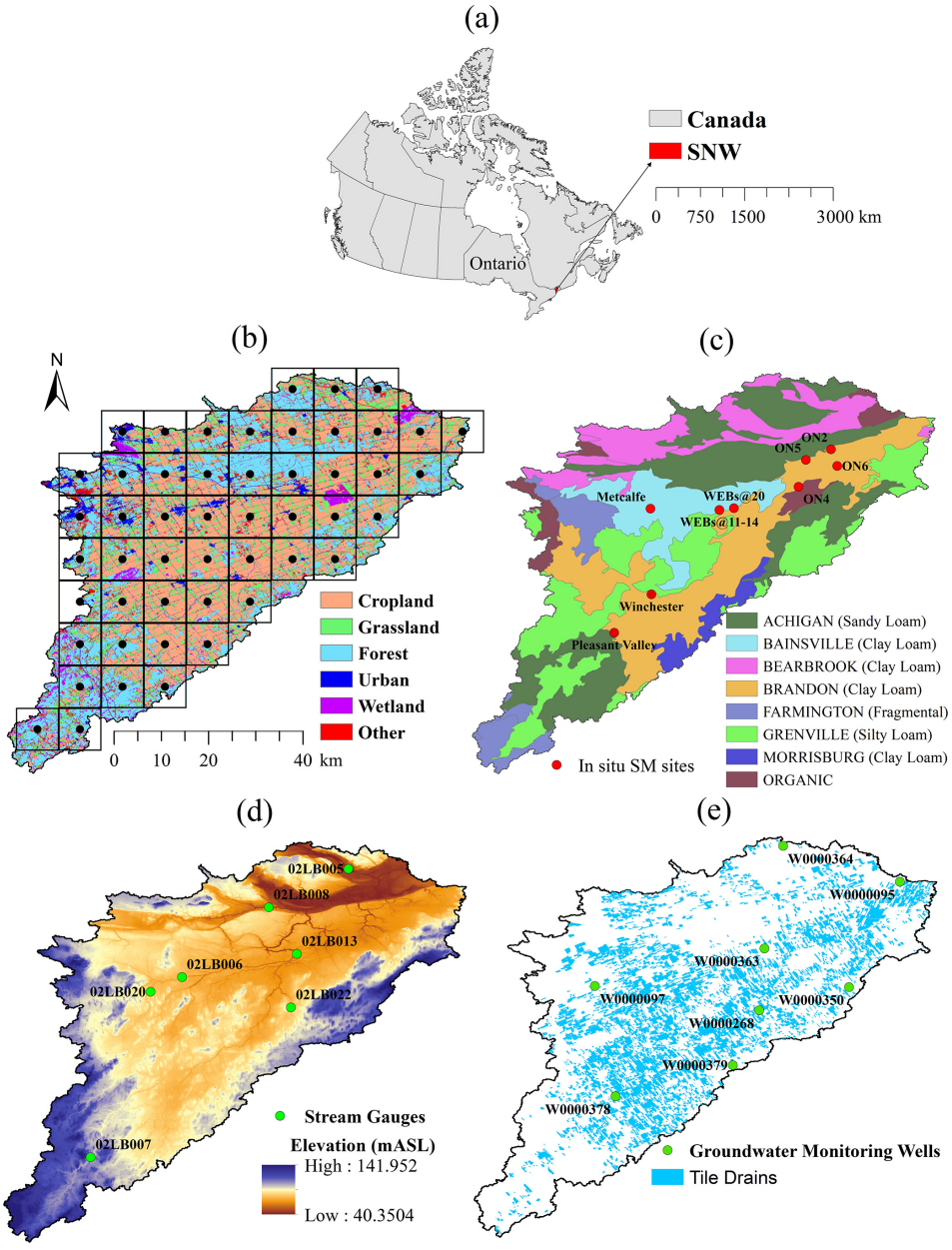

Figure 1. **(a)** Location of the South Nation Watershed (SNW). **(b)** The SNW land cover map (source: Agriculture and Agri-Food Canada's Annual Crop Inventory 2015) overlaid with location of the 9 km grids (boxes for the pixels and black dots for the centers) for the SMAP SM product used in this study. **(c)** Soil map for the SNW (source: Soil Landscapes of Canada version 3.2, Agriculture and Agri-Food Canada), along with the in situ SM monitoring sites. **(d)** Surface elevation along with location of streamflow gauges. **(e)** Tile drains installed for the SNW (provided by the South Nation Conservation Authority), along with location of groundwater level monitoring wells.

model subsurface domain, the three soil layers (0–25, 25–50, and 50–100 cm depths) of 3D elements were constructed by superimposing the four mesh layers of planar elements at the soil surface, 25, 50, and 100 cm depths, respectively. The four mesh soil layers of planar elements can provide the simulated SM at the four specific depths (soil surface, 25, 50, and 100 cm), while the three soil layers of 3D elements can provide the simulated SM for the depth intervals of 0–25, 25–50, and 50–100 cm. The simulated SM from the planar element mesh layer at the soil surface represents the simulated SSM. Underlying the three soil layers are the four hydrostratigraphic layers (three Quaternary layers and one bedrock layer), with geometry and lithology derived from Logan et al. (2009). The tile drains installed in the SNW (Fig. 1e) are not resolved in the model because of resolution constraints associated with the size of the model domain and the neces-

sity of carrying a practical number of finite elements. The influence of tile drainage absence in the model will be discussed in this study (Sect. 6.3).

Appropriate spin-up is essential for integrated surface-subsurface models (e.g., Ajami et al., 2014, 2015; Erdal et al., 2019). Similar to Frey et al. (2021), the HGS model herein was initialized following a three-step procedure. Firstly, the model was forced by long-term ($\sim$ 30-year) average annual net precipitation until steady-state groundwater heads and streamflow rates were established. Secondly, using a steady state as an initial condition, the model was forced by monthly normal liquid water flux and potential evapotranspiration for a decadal cycle, yielding a year over year dynamic equilibrium condition. Thirdly, using a dynamic equilibrium as an initial condition, the model was forced with daily transient liquid water flux and potential evapotranspiration derived from gridded daily climate data sets from Natural Resources Canada (NRCan) (McKenney et al., 2011) in combination with snow water equivalent data derived from the ERA5 land surface reanalysis product (Muñoz-Sabater et al., 2021). The daily transient simulations extended from 1 January 2008 to 31 December 2017 and were run multiple times, with model performance only evaluated after the second set of simulations. The model calibration primarily involved manually tuning the soil hydraulic conductivity and Manning's surface roughness coefficient for the 1D river/stream channels. The objective of calibration was to optimize surface water flow rates at the hydrometric stations (Fig. 1d) and groundwater levels at the monitoring wells (Fig. 1e). Subsequent analysis is based on the 31 March 2015 (the date when SMAP started operation) to 31 December 2017 time frame, using daily transient output data from the calibrated HGS model.

2.4 Comparison analysis and performance metrics

2.4.1 Evaluation of SMAP and modeled soil moisture

The SM estimates from the SMAP product and HGS model simulations are evaluated against the SM measurements from in situ monitoring sites (Fig. 1c). The specification of in situ SM measuring is provided in Table 1. Since the in situ SM sites are sparse, the evaluation is available only at point scale. SMAP SSM and HGS-simulated SSM estimates are evaluated using the 0–5 cm in situ SM measurements. The HGS-simulated root zone SM is evaluated at two depth profiles: 0–25 and 0–100 cm. In the 0–25 cm layer, the simulated SM in the model's top soil layer (0–25 cm) is compared to a depth-weighted average of in situ measurements in the top 25 cm soil (i.e., 5 and 25 cm depths at the Real-Time In-Situ Soil Monitoring for Agriculture (RISMA) sites, 10 and 20 cm depths at Metcalfe and Pleasant Valley, and 20 cm depth at Winchester stations; see Table 1). In the 0–100 cm layer, a depth-weighted average of simulated SM from the model's three soil layers (0–25, 25–50, and 50–100 cm depths) is evaluated against a depth-weighted average of in situ measurements in the top 100 cm soil (i.e., 5, 20, and 50 cm depths at the RISMA sites; 10, 20, and 50 cm depths at Pleasant Valley, and 15 and 45 cm depths at WEBs stations; see Table 1). At each in situ site, the unbiased root mean squared error (ubRMSE) and Pearson correlation coefficient (R) are computed based upon the daily time series using the following equations:

$$\mathrm{ubRMSE} = \sqrt{E[((\theta_\mathrm{s} - E[\theta_\mathrm{s}]) - (\theta_i - E[\theta_i]))^2]}, \quad (3)$$

$$R = E[(\theta_\mathrm{s} - E[\theta_\mathrm{s}])(\theta_i - E[\theta_i])](\sigma_\mathrm{s}\sigma_i)^{-1}, \quad (4)$$

where $E[\cdot]$ is the expectation operator. θ_s and θ_i indicate the daily time sequences of satellite (or model) soil moisture and in situ data, respectively. σ_s and σ_i denote the standard deviations of θ_s and θ_i, respectively.

2.4.2 Evaluation of HGS-simulated streamflow and GW level

The simulated streamflow rates and GW levels in the fully integrated modeling framework are physically linked to SM and GW flow and are hence also a reflection of water dynamics in the variably saturated subsurface domain. The simulated streamflow is evaluated using streamflow measurements from Water Survey of Canada (WSC) hydrometric stream gauges (Fig. 1d), and performance is assessed with the Nash–Sutcliffe efficiency (NSE) in Eq. (5):

$$\mathrm{NSE} = 1 - E[(Q_\mathrm{obs} - Q_\mathrm{sim})^2]/E[(Q_\mathrm{obs} - E[Q_\mathrm{obs}])^2], \quad (5)$$

where $E[\cdot]$ is the expectation operator. Q_obs and Q_sim indicate the daily time sequences of observed and simulated stream discharge values, respectively. NSE ranges from $-\infty$ to 1, with 1 as the optimal value.

The simulated GW levels are compared to GW level measurements provided by the Provincial Groundwater Monitoring Network (PGMN; https://data.ontario.ca/dataset/provincial-groundwater-monitoring-network, last access: September 2021) wells (Fig. 1e). Since the temporal variability information is of the most interest for the simulated GW levels in this study, the Pearson correlation coefficient (R) between the temporal variations of simulated and observed GW level anomalies is calculated at each GW monitoring well across the SNW. The GW level anomalies represent the departures from their respective average over the evaluation period (31 March 2015 to 31 December 2017).

2.4.3 Comparison between SMAP and HGS model simulations

The SMAP data (SSM and SWI) are compared to the HGS model simulations (SSM, subsurface SM, and GW storage) to quantify the vertical coupling and response time differences between satellite SM and the variably saturated subsurface water. The comparisons are made at both the 9 km (SMAP product grid) resolution and the entire watershed and

Table 1. Specification of in situ soil moisture stations.

Station ID	Latitude (°)	Longitude (°)	Sampling intervals	Measuring depths (cm)	Data period
[a]RISMA ON2	45.4016	−74.9479	15 min	0–5, 5, 20, 50	2015 to 2017
RISMA ON4	45.3140	−75.0193	15 min	0–5, 5, 20, 50	2015 to 2016
RISMA ON5	45.3769	−75.0031	15 min	0–5, 5, 20, 50, 100	2015 to 2017
RISMA ON6	45.3628	−74.9342	15 min	0–5, 5, 20, 50	2016 to 2017
Metcalfe	45.2626	−75.3439	Hourly	10, 20	2015 to 2017
Pleasant Valley	44.9726	−75.4237	Hourly	10, 20, 50	2017
[b]WEBs@11–14	45.2598	−75.1929	15 min	15, 45	2015 to 2017
WEBs@20	45.2639	−75.1607	15 min	15, 45	2015 to 2017
Winchester	45.0623	−75.3418	Hourly	20	2017

[a] Agriculture and Agri-Food Canada's Ontario Real-Time In-Situ Soil Monitoring for Agriculture (RISMA) stations.
[b] Agriculture and Agri-Food Canada's WEBs meteorological stations.

are measured using the unbiased root mean squared difference (ubRMSD), R, anomaly R, and Spearman's rank correlation (ρ), depending upon the variables under comparison. The ubRMSD and R are computed using the equations similar to Eqs. (3) and (4) but with the two variables from the SMAP and HGS simulation, respectively. The anomaly R calculation is similar to the R calculation but uses the anomaly time series of the variables, which are defined as departures of raw values from their monthly normals over the study period (2015–2017). For each variable, all 3-year (2015 to 2017) monthly data must be valid for computing the monthly normal of a calendar month. Spearman's rank correlation (ρ) is calculated as

$$\rho = 1 - \frac{6\sum d^2}{n\left(n^2-1\right)}, \tag{6}$$

where d represents the difference between the ranks of the SMAP and HGS model variables, and n denotes the length of data. In this study, ρ is used for timescale quantification for water transport from the surface soil layer to deeper unsaturated and saturated zones.

3 Evaluation of SMAP SSM and model simulations

The evaluation scores for the SMAP SSM and HGS SM across the individual in situ sites are listed in Table 2. In this study, the in situ SSM (0–5 cm) measurements are only available at Agriculture and Agri-Food Canada's Ontario Real-Time In-Situ Soil Monitoring for Agriculture (RISMA) stations (Table A1). Figure 2 shows the SSM time series from SMAP, HGS model, and in situ measurements at the four Ontario RISMA stations. Overall, both the SMAP and HGS modeling captured the in situ-observed SSM temporal variability very well (Fig. 2). Both the SMAP SSM and simulated SSM showed a mean ubRMSE of about 0.05–0.06 $m^3\ m^{-3}$ and a mean R of about 0.7 with the in situ measurements (Table 2). The performance of SMAP SSM over the SNW is

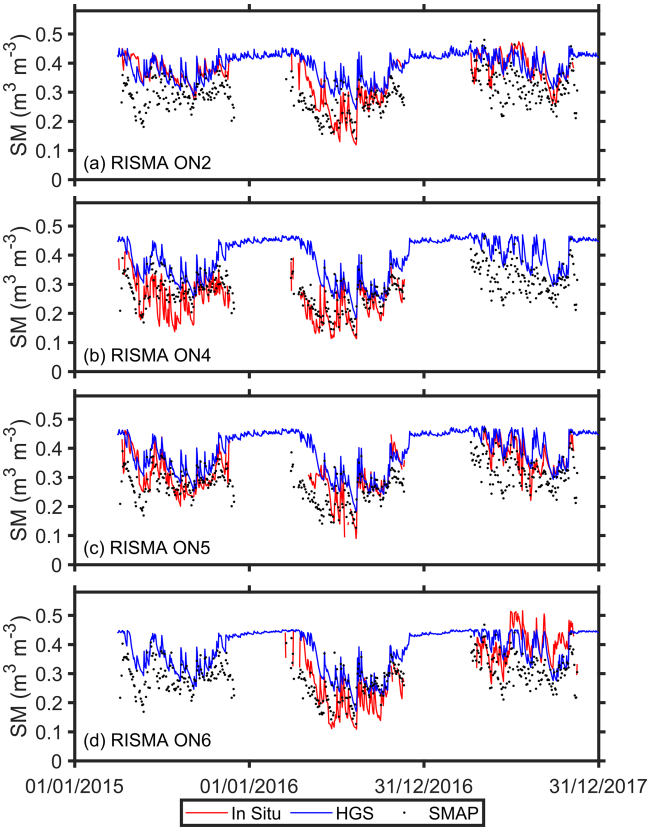

Figure 2. The SSM time series from SMAP, the HGS model simulation, and in situ measurements, respectively, at the four RISMA stations: **(a)** ON2, **(b)** ON4, **(c)** ON5, and **(d)** ON6.

very similar to that over the Great Lakes region (Xu, 2020; Xu and Frey, 2021), which is approximately adjacent to the study region SNW.

Figures A1 and A2 show the root zone SM time series comparison between HGS simulations and in situ measurements for the 0–25 and 0–100 cm soil layers, respectively.

Table 2. Soil moisture (SM) performance metrics. Bold font denotes average values.

Metrics	Station ID	SMAP	HGS SM		
		SSM	Near-surface	0–25 cm	0–100 cm
ubRMSE ($m^3\ m^{-3}$)	RISMA ON2	0.056	0.050	0.038	0.021
	RISMA ON4	0.047	0.061	0.047	0.028
	RISMA ON5	0.055	0.041	0.042	0.022
	RISMA ON6	0.079	0.066	0.040	0.030
	Metcalfe	–	–	0.053	–
	Pleasant Valley	–	–	0.024	0.013
	WEBs@11–14	–	–	–	0.023
	WEBs@20	–	–	–	0.035
	Winchester	–	–	0.033	–
	Average	**0.059**	**0.054**	**0.040**	**0.025**
R	RISMA ON2	0.67	0.76	0.74	0.76
	RISMA ON4	0.72	0.56	0.67	0.73
	RISMA ON5	0.66	0.82	0.75	0.86
	RISMA ON6	0.71	0.80	0.82	0.76
	Metcalfe	–	–	0.70	–
	Pleasant Valley	–	–	0.81	0.77
	WEBs@11–14	–	–	–	0.88
	WEBs@20	–	–	–	0.70
	Winchester	–	–	0.77	–
	Average	**0.69**	**0.74**	**0.75**	**0.78**

Overall, the HGS simulations agree with the in situ measurements very well in terms of the SM temporal variability in the two soil profiles across all available validation sites (Figs. A1 and A2), with the mean *R* close to or exceeding 0.75 for both soil profiles (Table 2). Unsurprisingly, the ubRMSE for the HGS soil moisture decreases with the increasing soil depth (Table 2), resulting from a smaller soil moisture temporal variability in a deeper profile (e.g., Albergel et al., 2008; Xu, 2020).

Figure A3 presents the simulated and observed hydrographs along with the calculated NSE values at the seven WSC streamflow gauges across the study watershed (as shown in Fig. 1d). The HGS simulations performed well in capturing the timing of peak flows. The NSE values are typically high, exceeding 0.62 for all gauges, although the underestimation of peak flows is also evident in the HGS hydrographs. A possible explanation for the flow underestimation is that the tile drain flow, which was not resolved in the present HGS model simulations, is also a source of discharge for streams (due to a shallow water table) in the real-world SNW. Further, the comparisons between the simulated and observed GW level anomalies at the eight GW monitoring wells were provided in Fig. A4. In general, the GW temporal variability was well reproduced by the HGS modeling across the monitoring wells, with *R* ranging from 0.4 to 0.86.

Overall, the SMAP SM product can capture the SSM variability well over the study region, while the HGS simulations match the observed surface and subsurface water dynamics well. This supports the HGS model's application towards quantifying the dynamic behavior of surface/subsurface hydrologic conditions and testing linkages between SMAP measurements and simulated water content in the variably saturated subsurface.

4 Comparisons between SMAP SSM and HGS model simulations

4.1 Comparison at the 9 km scale

In this section, we compare the SMAP SSM with the HGS-simulated SM at the SMAP product grid (9 km) scale. Since the HGS model has a higher resolution than the 9 km SMAP grid (see Sect. 2.3), the model SM estimates are spatially aggregated (i.e., averaged) within each SMAP grid cell. Figure 3a illustrates the ubRMSD values across all SMAP grids for the SMAP SSM and HGS SSM comparison, with the summarized ubRMSD provided in Fig. 4a. The SMAP grid-scale ubRMSD values range from 0.04 to 0.06 $m^3\ m^{-3}$ and are typically lower in the forested areas than over the agricultural fields (Fig. 3a with the land cover map provided in Fig. 1b). The average ubRMSD between the SMAP and HGS SSM estimates is about 0.047 $m^3\ m^{-3}$ at the 9 km scale (Fig. 4a).

Figure 3b shows the *R* values between the SMAP SSM and the HGS-simulated SSM across all individual SMAP grids, which are summarized using the box plot in Fig. 4b. The simulated SSM can capture the SMAP-observed SSM

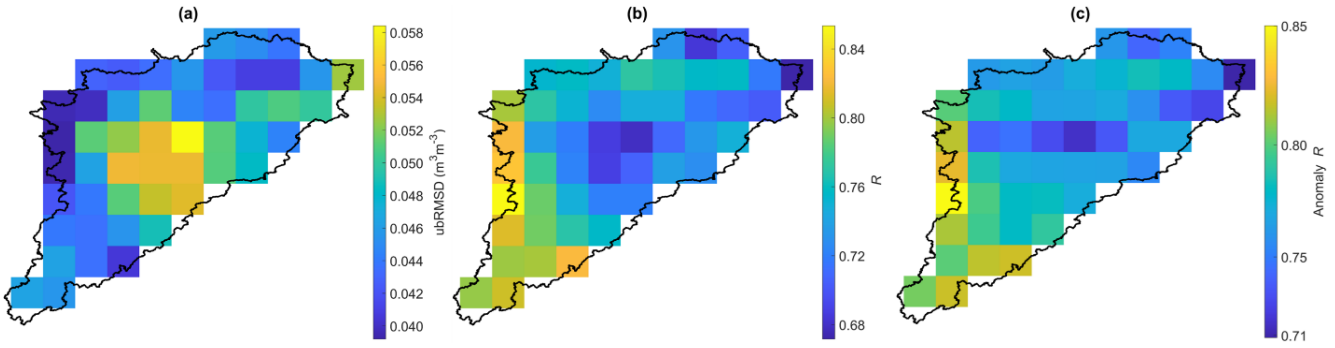

Figure 3. **(a)** ubRMSD, **(b)** R, and **(c)** anomaly R between the SMAP SSM and HGS SSM across all SMAP grids.

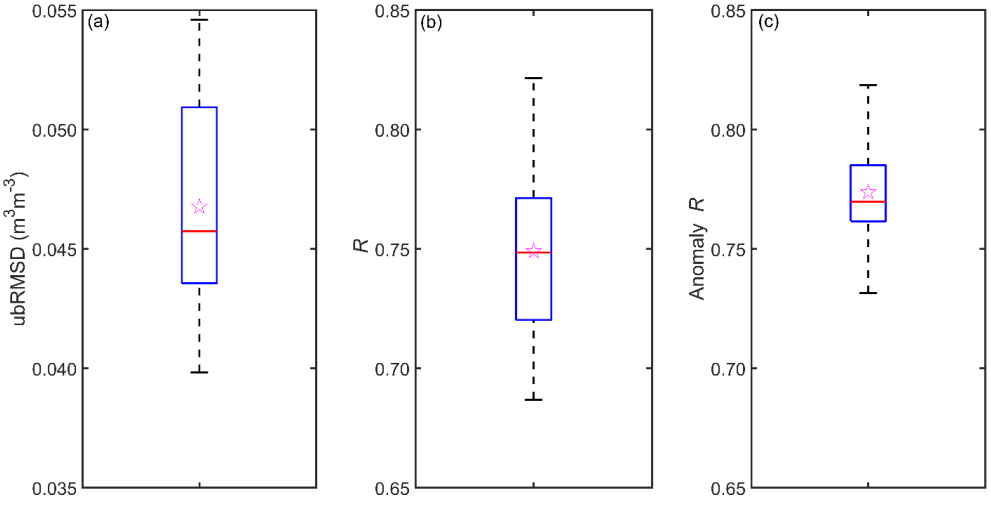

Figure 4. Box plots of **(a)** ubRMSD, **(b)** R, and **(c)** anomaly R between the SMAP SSM and HGS SSM, summarized from all 9 km grids within the study watershed. Within each box, the horizontal segment and the star denote the median and mean of the sample data, respectively; the lower and upper edges of the box indicate the 25th and 75th percentiles, respectively; and the bottom and top ends of the whiskers denote the 5th and 95th percentiles, respectively.

dynamics quite well at the 9 km grid scale, with an average R exceeding 0.7 (Fig. 4b). In terms of the spatial variability, the R values are typically higher over the forests than their counterparts over the agricultural lands (Fig. 3b), which may be in part due to tile drainage not fully captured by the model (see Sect. 6.3). The anomaly R results (Figs. 3c and 4c) are similar to the R results, indicating that the obtained correlations between SMAP and the HGS model are dominated by the day-to-day variations (rather than the seasonal trends) in the SM time series. Further, the linear regression between SMAP SSM (independent variable) and HGS SSM (dependent variable) suggests that modeled SSM is systematically wetter than SMAP SSM (intercept >0) but shows a smaller change in response to every unit change in SMAP SSM (slope <1) across the watershed (Figs. A5 and A6).

To examine the linkage between SMAP SSM and water storage variability in the deeper subsurface, time-lagged cross-correlations between the SMAP SSM and simulated subsurface SM and GW storage were calculated for each 9 km grid. Here Spearman's rank correlation (rather than the Pearson correlation) is used for the time-lagged cross-correlation analysis since the monotonic (rather than linear) relationship is of the most interest for identifying the phase difference between near-surface and deeper subsurface water content variability. Figure 5 presents Spearman's rank correlations (the 5th to 95th percentiles from all SMAP grids over the study watershed) between the time series of SMAP SSM and the HGS-simulated subsurface SM (0–25, 25–50, and 50–100 cm depths) and GW storage for a time lag ranging from 0 to 60 d. The optimal time lags (in days) and corresponding highest Spearman's rank correlations across all SMAP grids are provided in Figs. A7 and A8, respectively.

Unsurprisingly, the simulated SM in the 0–25 cm depth (Figs. 5a and A7a) showed simultaneous response (a time lag of 0 d) to the SSM variability captured by SMAP across the study watershed. By contrast, simulated water content variations in the deeper subsurface showed a delayed response relative to the SMAP SSM variability. The optimal time lag

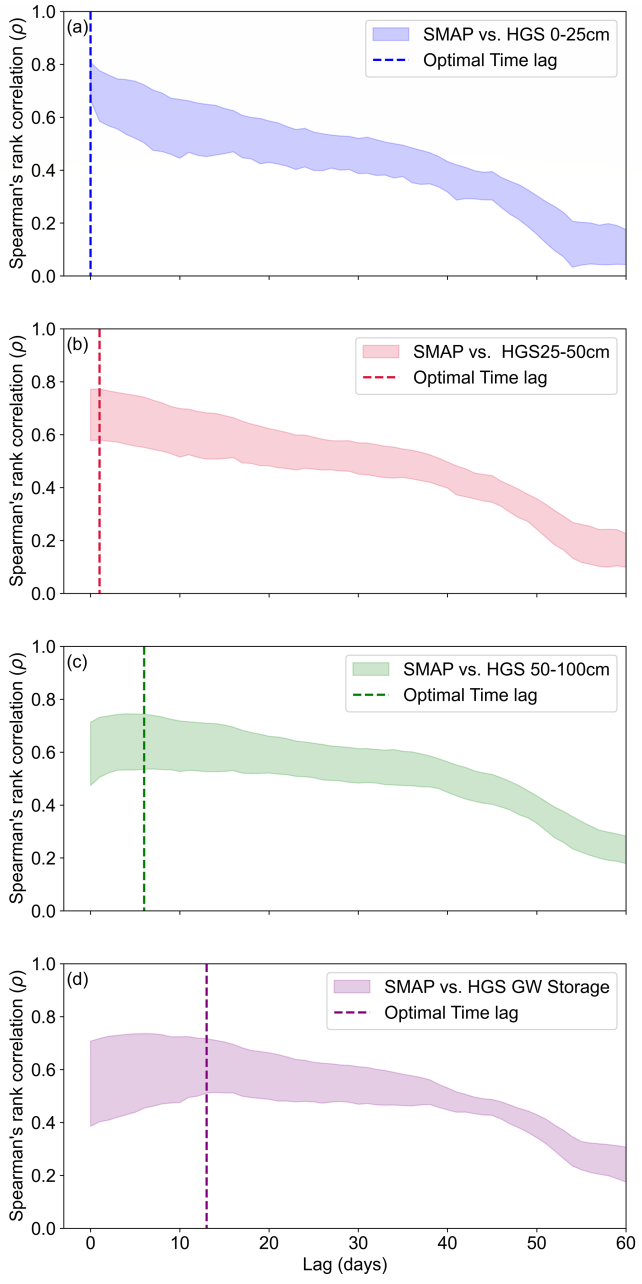

Figure 5. Spearman's rank correlation coefficients between the time series of SMAP SSM and HGS-simulated SM from **(a)** 0–25 cm depth, **(b)** 25–50 cm depth, and **(c)** 50–100 cm depth, respectively, as well as **(d)** GW storage for time lags ranging from 0 to 60 d. Positive lags indicate that the SMAP data are leading the HGS simulations. In each plot, the shaded band represents the 5th to 95th percentiles of the results from all SMAP grids within the study watershed. For each SMAP grid, the optimal time lag is defined as the one with the maximum Spearman's rank correlation between SMAP SSM and HGS-simulated variable. The vertical dashed line indicates the median of the optimal time lags from all SMAP grids.

increased with depth, with a median delay of about 1–2 d for the 25–50 cm SM (Fig. 5b), about 6 d for the 50–100 cm SM (Fig. 5c), and about 11–12 d for the GW storage (Fig. 5d).

By comparing the spatial distribution of time lags on a SMAP grid cell basis (Fig. A7) to the soil distribution (Fig. 1c), the time delay for deeper zones is typically shorter in regions with well-drained soils (e.g., the southwestern portion of SNW) than in areas with poorly or imperfectly drained soils (e.g., the northern SNW), reasonably reflecting the impact of soil properties on deeper subsurface hydrologic response. Table A1 provides the average optimal time lags for the six major soils over the study watershed. For each soil, the averaged optimal time lag is calculated using the 9 km SMAP grids dominated by the soil texture (the Organic and Morrisburg soils are not calculated and included in the table due to their insufficient sample grids). Clearly, the soil drainage has a key impact on the spatial variability of the time lags for deeper layers. The optimal time lag for the 25–50 cm depth is statistically shorter (longer) than 1 d in regions with well-drained (imperfectly or poorly drained) soils. Moving to the 50–100 cm depth, on average, the soils of Achigan-dominated (imperfectly drained) and Bearbrook-dominated (poorly drained) regions experienced the longest optimal time delay (close to or higher than 10 d). Further, the optimal time delay is statistically less (more) than 10 d for the GW system in the areas with good (poor or imperfect) soil drainage. It should also be noted that the quantified time delay in deep subsurface water dynamics did not explicitly account for the impact of tile drainage due to the absence of tile drains in the model. The maximum correlations (corresponding to the optimal time lags) between the SMAP SSM and simulated subsurface water also showed a clear spatial pattern, with higher values in the southwestern SNW (Fig. A8), which corresponds to the regions with well-drained soil (Grenville and Farmington soils in Fig. 1c). Overall, the soil texture showed an important impact on the vertical coupling length (correlations) and response time differences between satellite SSM and the variably saturated subsurface water.

4.2 Comparison at the watershed scale

Figure 6 compares the SMAP and HGS-simulated time series for the watershed-averaged SSM. Although the simulated SSM is systematically wetter than SMAP SSM, the simulated results match the SMAP measurements very well in terms of SSM variations, with both the R and anomaly R between them exceeding 0.8 and an ubRMSD of less than 0.04 $m^3\ m^{-3}$. The observed mean biases between the SMAP and modeled SSM may in part be related to the calibration of the SMAP SM retrieval algorithm. Although the SMAP SM retrievals can capture the SSM variability very well, they typically show an underestimation of SSM (i.e., drier surface soils) over Canadian agricultural regions due to issues with correcting the effects of growing vegetation (e.g., Collian-

der et al., 2017). In addition, the absence of tile drainage in the HGS model could cause a wet bias over the tile drained landscape ($\sim 25\,\%$ of the entire watershed) and therefore moderately increase the wetness of the simulated watershed-averaged SSM. Given the scarcity of in situ SM measurements, this study is unable to investigate whether the SMAP retrieval algorithm or the modeling should be blamed for the bias. However, such bias has a negligible effect on this study since the SM temporal variations from the SMAP and HGS model are of primary interest herein.

The relationships between variations of SMAP SSM and HGS-simulated water content in deeper unsaturated/saturated zones at the watershed scale are quantified in Fig. 7. Figure 7a shows the time series of the simulated watershed-averaged SM in the 0–25, 25–50, and 50–100 cm depths and watershed-integrated GW storage, in comparison with the watershed-averaged SMAP SSM. Spearman's rank correlations between the SMAP SSM and the HGS-simulated subsurface water for time lags ranging from 0 to 60 d are provided in Fig. 7b. Variations in simulated subsurface water are highly correlated across the different depth intervals. The surface soil layer (0–25 cm) is directly impacted by influxes and effluxes of water and therefore shows the largest day-to-day water content variability, while the 50–100 cm SM and GW storage show comparably smoother day-to-day fluctuations (Fig. 7a). Accordingly, in Fig. 7b, variations in time-lagged correlation between SMAP SSM and simulated subsurface water become smoother as the subsurface depth increases, which also reflects the gradual filtering of high-frequency signals in subsurface water content with the increasing depth.

Very good agreement is observed between the variations of the watershed-averaged SMAP SSM and HGS-simulated watershed-averaged surface layer (0–25 cm) SM, with their highest Spearman's rank correlation coefficient reaching around 0.8, which occurs at a time lag of 0 d (i.e., the delay is less than 1 d and cannot be resolved at daily time steps). With the time lag increasing, the correlation between SMAP SSM and the simulated 0–25 cm SM drops rapidly (green in Fig. 7b). The variations of deeper subsurface SM and GW storage are also in relation to the SMAP SSM variability but show a delayed response. At the watershed scale, the 25–50 cm SM, 50–100 cm SM, and GW storage showed the highest Spearman's rank correlation with the SMAP SSM variability at a temporal delay of ~ 1, ~ 6, and ~ 11 d, respectively (Fig. 7b), which is very similar to the analysis at the 9 km scale (Fig. 5).

In Fig. 7a, the SMAP SSM (top 5 cm) indicated a slightly earlier thaw onset than the model-simulated SM in deeper layers. This reflects a downward heat transfer and migration of thawing front. During a thawing/warming period, the soils typically have a downward temperature gradient (i.e., soil temperature decreases with increased soil depth), which causes a downward heat transfer and migration of thawing front. The thaw onset difference between different depths is consistent with the response time differences between satellite SSM and the subsurface water.

5 Comparisons between SMAP-derived SWI and HGS model simulations

5.1 SMAP SWI estimation based upon classic time length T

The linkage between SMAP SSM-derived SWI and HGS simulations is investigated here. Firstly, SWI based upon the model-independent characteristic time length T (so that the calculated SWI is entirely independent of the model simulations) is compared to simulated subsurface SM. It must be acknowledged that ideally, the time length T (model-independent) should be estimated using in situ SM measurements (e.g., Wagner et al., 1999, Tian et al., 2020). However, given the scarcity of in situ SM data and the relatively large spatial scale of the analysis herein, it is not possible to determine the time length T (model-independent) based upon evaluation with in situ data. To this end, $T = 15$ d and $T = 20$ d (taken from Wagner et al., 1999), which represent the classic T values for SWI estimation in the surface soil layer (0–20 cm) and the root zone soil layer (0–100 cm), respectively, were used for calculating the model-independent SWI across the 9 km grids. The calculated SWI using $T = 15$ d is compared to the HGS 0–25 cm SM, while the calculated SWI using $T = 20$ d is compared to the HGS 0–100 cm SM. Figure A9 presents the ubRMSD, R, and anomaly R between SWI and HGS-simulated subsurface SM across all 9 km grids. The 9 km grid-scale evaluation metrics are summarized in Fig. 8. Across the SNW, the 9 km scale ubRMSD between SWI and HGS SM typically ranges from 0.03 to 0.05 $m^3\,m^{-3}$ (with an average of 0.035 $m^3\,m^{-3}$) for the top 25 cm layer (Figs. 8a and A9a) and less than 0.04 $m^3\,m^{-3}$ (with an average of about 0.03 $m^3\,m^{-3}$) for the top 100 cm layer (Figs. 8a and A9b). In the two soil depths (top 25 cm and top 100 cm), both the R and anomaly R between SWI and HGS SM are very high and typically exceed 0.70 (Fig. A9c–f), with their means exceeding 0.82 (Fig. 8b and c).

Further, the SWI time series are calculated from the watershed-averaged SMAP SSM series (using $T = 15$ d and $T = 20$ d, respectively) and are then compared with the watershed-averaged HGS SM (top 25 cm and top 100 cm, respectively) (Fig. 9). The SWI time series represent the simulated SM variability in the two soil layers very well, with an R value close to 0.9. Unsurprisingly, for both soil depth intervals (top 25 cm and top 100 cm), the simulated SM showed a higher correlation with the SWI than with the SMAP SSM (Fig. 9).

Figure 10 presents the comparison of variations in the HGS-simulated watershed-integrated GW storage and the watershed-scale SWI in the 0–100 cm soil (using $T = 20$ d).

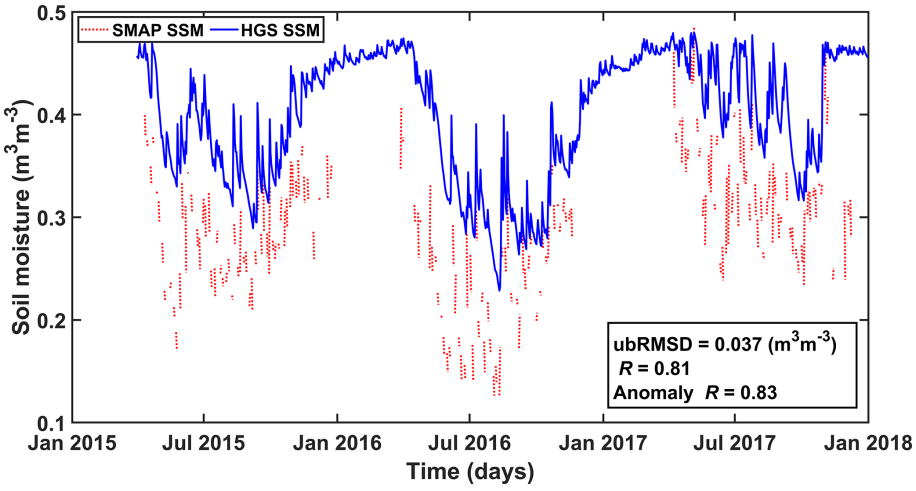

Figure 6. Comparison between the SMAP and HGS simulations for the watershed-averaged SSM time series.

The SWI and GW storage share very similar temporal variations, with their best correlation occurring at a time lag of about 2 d. This may demonstrate the potential of SWI to predict the day-to-day variations in GW.

5.2 Identification of optimal characteristic time length T_{opt}

Although the optimal characteristic time length T_{opt} for SWI estimation has been investigated for many regions across the world (e.g., Bouaziz et al., 2020; Ceballos et al., 2005; Tian et al., 2020; Wagner et al., 1999; Zhang et al., 2017), Canadian agricultural watersheds are typically underrepresented in this regard. In this part, T_{opt} is identified for the study watershed by optimally matching variations in SWI and HGS-simulated subsurface SM. First, at each SMAP grid, SWI is calculated from the SMAP SSM series for the characteristic time length T varying between 1 and 100 d. Then, Spearman's rank correlations between the SMAP-derived SWI for each value of T and the HGS-simulated subsurface SM (from three depth intervals: 0–25, 0–50, and 0–100 cm) are calculated. For each depth interval, the T value corresponding to the highest Spearman's rank correlation is defined as the optimal T_{opt}. The optimal T_{opt} (in days) and the associated highest Spearman's rank correlations across all SMAP 9 km grids are provided in Fig. A10. A comparison between Fig. A10 and the soil map (Fig. 1c) indicates that the spatial variability of T_{opt} is impacted by the soil texture. T_{opt} is typically longer for the landscape with poorly (e.g., Bearbrook) or imperfectly (e.g., Achigan) drained soils than for regions with well-drained soils (e.g., Farmington). Table A2 shows the average T_{opt} for the six major soils over the study watershed. For each soil, the averaged T_{opt} is calculated using the 9 km SMAP grids dominated by the soil texture (the soils of Organic and Morrisburg are not calculated and included in the table due to their insufficient sample grids). Clearly, the spatial variability of T_{opt} is strongly related to the soil drainage class. For the three depth intervals, 0–25, 0–50, and 0–100 cm layers, on average, T_{opt} exceeds 20, 24, and 30 d, respectively, in regions with imperfect or poor soil drainage, while the T_{opt} values are reduced to below 18, 21, and 28 d, respectively, for the well-drained soils.

The frequency distribution of T_{opt} at the 9 km grid scale is provided in Fig. A11, while Fig. 11a presents Spearman's rank correlations (the 5th to 95th percentiles from all SMAP grids over the study watershed) between the HGS-simulated SM (0–25, 0–50, and 0–100 cm depths, respectively) and the SWI using T from 1 to 100 d. Across the SNW, the 9 km grid-scale T_{opt} ranges largely from 14 to 26 d (Fig. A11a) with a median of 21 d (Fig. 11a) for the 0–25 cm layer, from 20 to 32 d (Fig. A11b) with a median of 24 d (Fig. 11a) for the 0–50 cm layer, and from 26 to 43 d for the 0–100 cm (Fig. A11c) with a median of 31 d (Fig. 11a) for the 0–100 cm layer. On average, T_{opt} increases with depth in the soil profile, which agrees with previous studies (e.g., Wagner et al., 1999; Tian et al., 2020; Zhang et al., 2017).

The maximum Spearman's rank correlations between SWI and simulated subsurface SM (0–25, 0–50, and 0–100 cm layer) typically exceed 0.8 at the 9 km scale (Figs. A10b, d, and f). By comparing Fig. A10 and the land cover map (Fig. 1b), the forested area typically shows higher maximum Spearman's rank correlations between the SWI and simulated subsurface SM than the agricultural fields, which again can be at least partially related to the absence of discretely resolved agricultural tile drainage in the model (see Sect. 6.3).

Figure 11b provides Spearman's rank correlations between watershed-averaged HGS subsurface SM and the SWI estimated from watershed-averaged SMAP SSM for T varying from 1 to 100 d. The watershed-scale T_{opt} is about 19, 30, and 38 d for the 0–25, 0–50, and 0–100 cm layers, respectively, showing a clear increase in T_{opt} with increased soil depth (Fig. 11b). Across the three layers, the watershed-scale T_{opt}

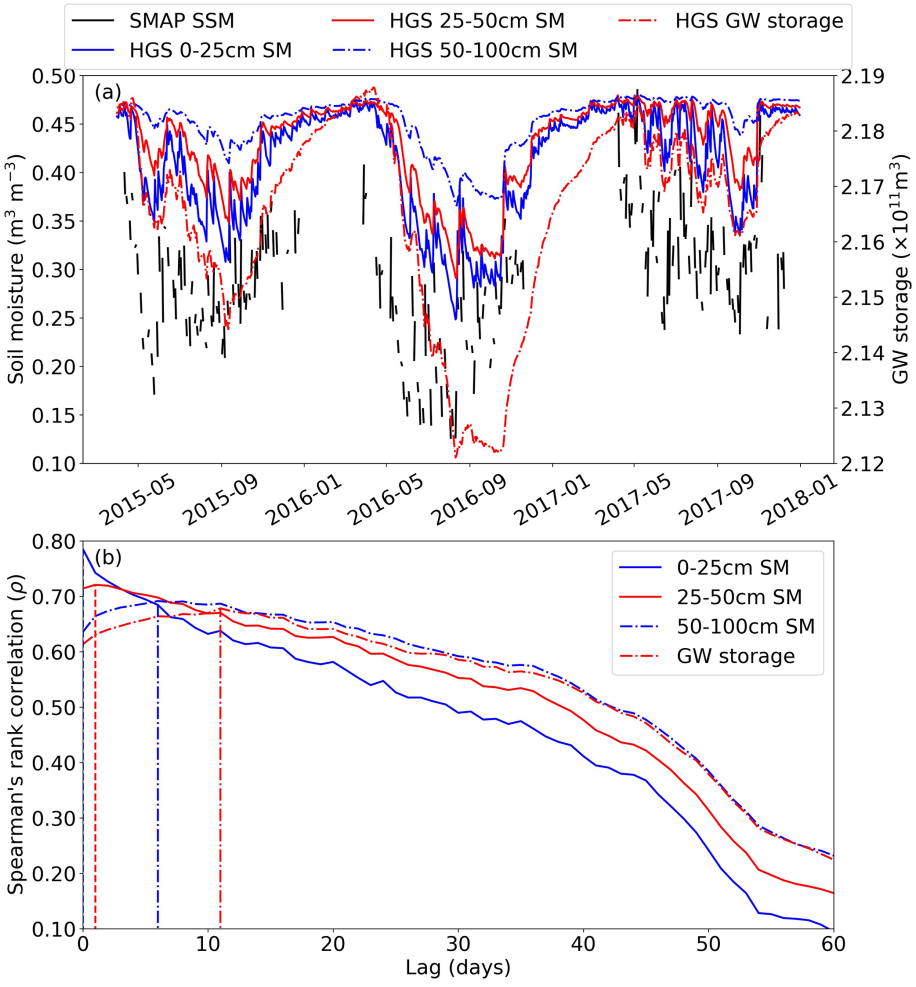

Figure 7. **(a)** Daily time series of HGS-simulated watershed-averaged SM in the 0–25, 25–50, and 50–100 cm depths and watershed-integrated GW storage, along with watershed-averaged SMAP SSM. **(b)** Spearman's rank correlation between the watershed-averaged SMAP SSM versus the HGS-simulated watershed-averaged 0–25, 25–50, 50–100 cm SM and watershed-integrated GW storage, respectively, for a time lag ranging from 0 to 60 d. Positive lags indicate that SMAP data lead the HGS simulations. In panel **(b)**, for each pair of comparisons, a vertical dashed line is provided to indicate the location of the optimal time lag corresponding to the maximum Spearman's rank correlation.

falls within the range of the most frequently occurring T_{opt} at the 9 km scale (14 to 26 d for the 0–25 cm layer, 20 to 32 d for the 0–50 cm layer, and 26 to 43 d for the 0–100 cm layer as indicated in Fig. A11), indicating no significant change in T_{opt} across the two spatial scales.

In addition, note that at both spatial scales and across the three layers, the correlations between the calculated SWI and modeled SM are very strong for a range of T values surrounding T_{opt}. For example, the simulated 0–100 cm SM shows a correlation >0.9 with SWI for T ranging from 19 to 60 d at the watershed scale (Fig. 11b), while a correlation >0.8 can be obtained between the simulated 0–100 cm SM and SWI for T ranging from 12 to 68 d at the 9 km scale (Fig. 11a). The selected model-independent value of $T = 20$ d for the 0–100 cm layer SWI (Sect. 5.1) falls within both T ranges and is therefore suitable for the 0–100 cm SWI estimation at both spatial scales (Figs. 8 and 9). Similarly, the selected model-independent value of $T = 15$ d for the 0–25 cm layer SWI is also suitable for both spatial scales.

6 Discussion

6.1 Novelty and improved understanding of near-surface–subsurface water interaction

This study quantified the potential of using SMAP SSM variability to predict subsurface water dynamics using two independent analysis approaches. The first approach is based upon the time-lagged cross-correlation in SM variations between the near-surface and deeper soil layers (e.g., Mahmood and Hubbard, 2007; Mahmood et al., 2012; Wu et al., 2002), which can be used to quantify if the subsurface SM variabil-

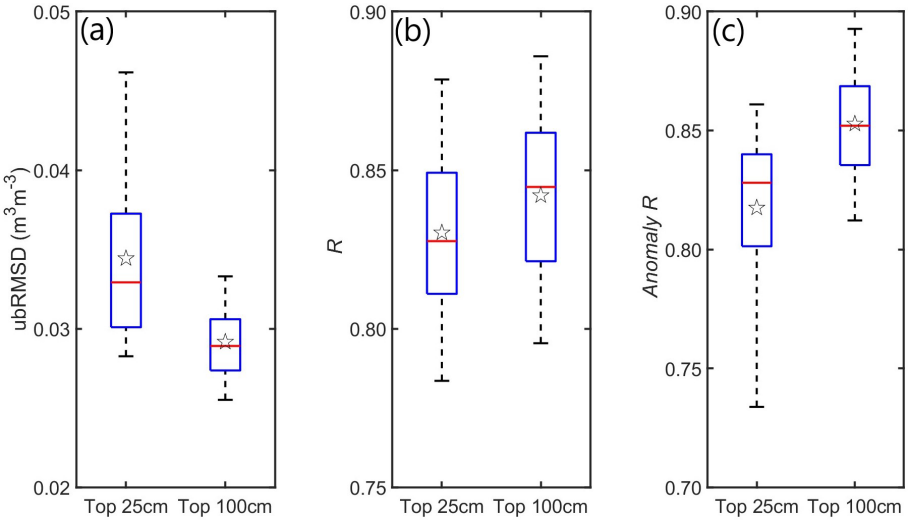

Figure 8. **(a)** Box plots for the ubRMSD between the SMAP SSM-derived SWI (using $T = 15$ d) and HGS-simulated top 25 cm SM and the ubRMSD between the SMAP SSM-derived SWI (using $T = 20$ d) and HGS-simulated top 100 cm SM, respectively, summarized from all SMAP 9 km grids over the study watershed. Within each box, the horizontal segment and the star denote the median and mean of the sample data, respectively; the lower and upper edges of the box indicate the 25th and 75th percentiles, respectively; and the bottom and top ends of the whiskers denote the 5th and 95th percentiles, respectively. Panels **(b)** and **(c)** are similar to panel **(a)** but for the correlation coefficient R and anomaly R, respectively.

ity could be approximated by delaying the temporal variations in satellite/SMAP SSM. The second approach focuses upon the SWI and optimal characteristic time length estimation, which investigates if the subsurface water content variability can be estimated by smoothing the satellite/SMAP SSM time series with an exponential filter (e.g., Bouaziz et al., 2020; Ceballos et al., 2005; Ford et al., 2014; Paulik et al., 2014; Tian et al., 2020; Wagner et al., 1999). Either analysis approach can be independently used to evaluate the linkage between the SMAP/satellite SSM variability and the deeper subsurface water content fluctuations. Both approaches indicate that the SMAP/satellite SSM variability is strongly linked to the deeper subsurface water content fluctuations and can be used to predict or infer subsurface SM and groundwater variability. Both the optimal time lag (for the delaying method) and the optimal characteristic time length (for the smoothing method) typically increase with soil depth and are mainly impacted by the soil drainage properties.

The novelty and advances provided by the study herein are as follows. Firstly, there is growing recognition that high-resolution integrated surface water–soil moisture–groundwater modeling and forecasting is crucial for landscape-scale water resource management (e.g., Simmons et al., 2020, and references therein). However, the assessment of large-scale (i.e., watershed to river basin), high-resolution integrated hydrologic simulations is often difficult due to a lack of spatially distributed observational information. This study attempts to fill this gap by presenting state-of-the-art satellite (SMAP) SM products as a tool for evaluating integrated hydrologic simulations. The investigation indicates that the SMAP product and the fully integrated hydrologic model simulations are matched very well in terms of the near-surface (top few centimeters) SM variability at both the 9 km scale and the watershed scale. Further, the simulated deeper subsurface SM and GW storage fluctuation is lagged and smoothed in relation to the SSM variability captured by SMAP. The quantified connections between satellite measurements and modeling results demonstrate the capability of the fully integrated hydrologic model to reproduce water content in the variably saturated subsurface domain at a spatial scale that aligns with SMAP cell size. The application of SMAP towards high-resolution fully integrated surface water–groundwater simulations expands upon previous inter-comparisons of satellite SM and simulations produced by land surface models (e.g., Al-Yaari et al., 2014; Dorigo et al., 2010; Draper et al., 2013; Parrens et al., 2012) or lumped models (e.g., Bouaziz et al., 2020).

Secondly, the study of coupling between near-surface–subsurface water fluctuations was extended to the saturated zone (GW) and investigated at multiple spatial scales in this work. In previous work, vertical coupling analyses typically included only the unsaturated zone (surface SM versus root zone SM) for point-scale or small catchments. For example, Mahmood and Hubbard (2007) and Mahmood et al. (2012) quantified the coupling and time lags between near-surface and root zone SM dynamics at the point or field scale in the US state of Nebraska and suggested that the strength of the coupling was subject to soil type, land use type, and climate, with the temporal delay ranging from several days to a few months. Herein, the high-resolution integrated model

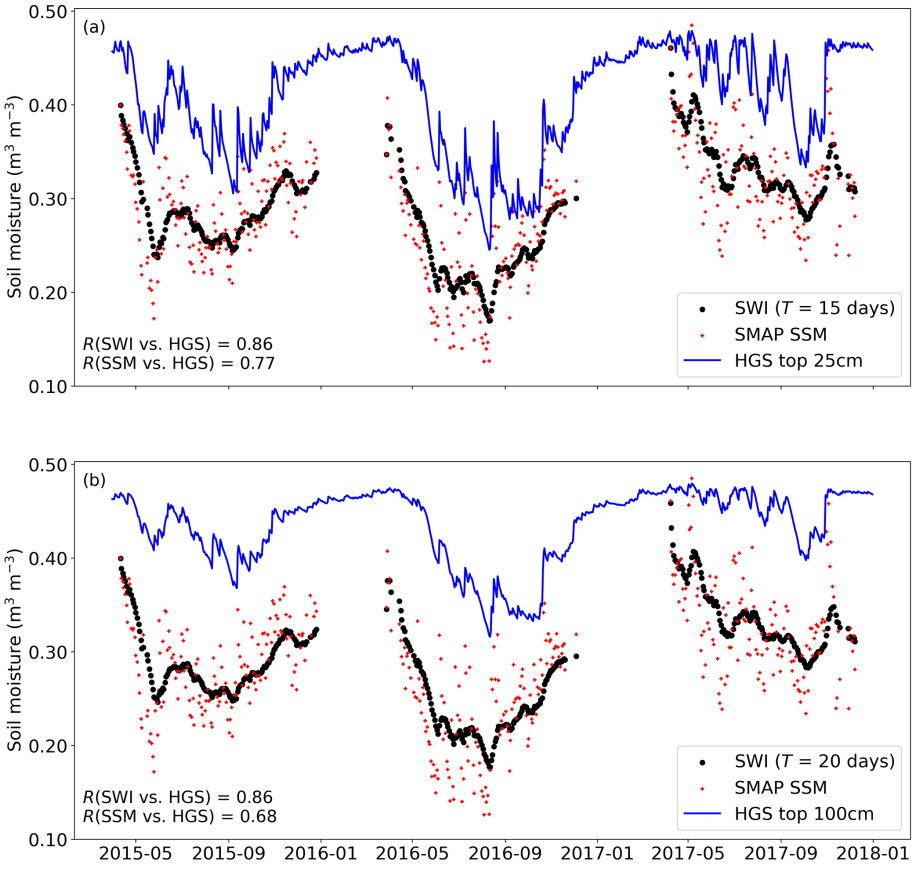

Figure 9. (a) Watershed-scale time series of SMAP SSM, SMAP SSM-derived SWI (using $T = 15$ d), and HGS-simulated top 25 cm SM. **(b)** Watershed-scale time series of SMAP SSM, SMAP SSM-derived SWI (using $T = 20$ d), and HGS-simulated top 100 cm SM. In each plot, the correlation R between SWI (or SMAP SSM) and simulated SM is provided.

simulations enabled an investigation on the vertical coupling and response time differences between dynamics of satellite SM and subsurface water in both unsaturated and saturated zones (i.e., variably saturated subsurface water) at both the 9 km grid scale and the watershed scale. Results from the two spatial scales showed consistent variation in vertical coupling and response time across different layers. At both scales, root zone SM and GW fluctuation can be approximated by shifting the SMAP SSM time sequences forward by a soil-property-dependent optimal time length that increases with subsurface depth. Over the SNW, where poorly or imperfectly drained soils dominate the agricultural regions, the optimal time lag (relative to the SSM variability) is about 1 d for the 25–50 cm SM, about 6 d for the 50–100 cm SM, and about 11 d for the GW storage at both scales. These findings have important implications for exploiting the potential of SMAP (or other satellite) SSM measurements for estimating subsurface water dynamics in deeper unsaturated and saturated zones. In particular, large-scale satellite SSM monitoring could provide a quick approach for predicting deeper subsurface water storage changes at continental or global scales and alleviate the need for hydrologic modeling in some types of investigations.

Thirdly, this work suggests optimal and appropriate time length T values for satellite-based SWI estimation and provides insight into linkages between SWI and subsurface water variability in both unsaturated and saturated zones over a representative Canadian agricultural watershed. Since T_{opt} for SWI estimation is dependent on a number of factors, including subsurface depth of interest, soil properties (e.g., Ceballos et al., 2005; de Lange et al., 2008; Wang et al., 2017), climate (e.g., Albergel et al., 2008; Mahmood et al., 2012; Wang et al., 2017), and land cover/land use (Bouaziz et al., 2020; Mahmood and Hubbard, 2007), characterization of T_{opt} has been extensively studied. As pioneers of the SWI approach, Wagner et al. (1999) recommended a T_{opt} of 15 and 20 d for the top 20 cm layer and top 100 cm layer, respectively, based on satellite and in situ SM monitoring over Ukraine. Zhang et al. (2017) reported a T_{opt} of 8 d for the 25 cm depth and 49 d for the 75 cm depth based upon in situ measurements in the US state of Oklahoma. Bouaziz et al. (2020) indicated that T_{opt} values varied significantly across different regions, and when using the SMAP

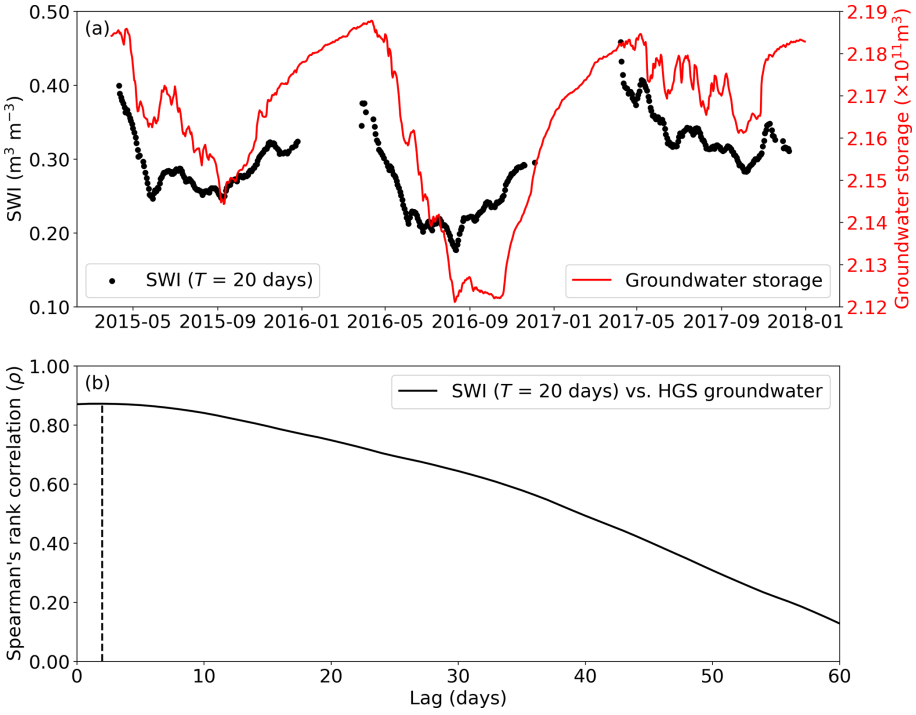

Figure 10. (a) Daily spaced time series of watershed-scale SWI (using $T = 20$ d) and HGS-simulated watershed-integrated GW storage. **(b)** Spearman's rank correlations between the two time series in panel **(a)** for a time lag ranging from 0 to 60 d. Positive lags indicate that the SWI leads the GW. In panel **(b)**, the vertical dashed line indicates the location of the time lag leading to the maximum Spearman's rank correlation between the two series.

SPL3SMP-E SM product (also used in the present study), T_{opt} values ranged from ∼ 2 to 42 d (within the 5 % to 95 % percentiles), with a median of around 25 d across their 16 study catchments in France. Tian et al. (2020) obtained a median T_{opt} of 10 d for the top 70 cm layer using SMAP SSM across in situ SM monitoring sites in the Heihe River basin, China. Canadian agricultural areas are typically underrepresented in previous SWI-related studies, and hence the present study helps fill this gap. In this study, the obtained optimal T_{opt} values for the entire root zone (0–100 cm layer) at the watershed scale (∼ 38 d) and for the majority of the 9 km grid cells (26 to 43 d) over the SNW are similar to those quantified in other agricultural regions (e.g., Bouaziz et al., 2020; Ceballos et al., 2005). The spatial variability of 9 km scale T_{opt} reasonably reflected the impact of soil texture. Note that at both scales (9 km and watershed) there is a range of T values surrounding T_{opt} that produce high correlations between the calculated SWI and modeled subsurface SM. As such, subsurface moisture variability over the SNW can be well represented by the SMAP-derived SWI using the classic T values (15 and 20 d for the 0–20 and 0–100 cm layers, respectively). The analysis of optimal (and appropriate) time length T values in this study provides important guidance for SWI estimation over Canada and other agricultural regions around the world. Furthermore, GW storage showed a similar but slightly delayed day-to-day variation relative to SMAP-derived SWI in the 0–100 cm layer, which further supports the use of satellite-derived SWI for detecting GW changes over a range of different timescales (e.g., Sutanudjaja et al., 2013).

6.2 Point-scale analysis

With the in situ soil moisture measurements at the four RISMA stations, the time lags between the variations of SSM (top 5 cm) and subsurface SM at the point scale are investigated and presented in Fig. A12 (other in situ sites are not used since they do not provide the SSM measurements). The optimal time lag is less than 1 d between the SSM and 20 cm depth SM at all four RISMA stations, consistent with the vertical coupling between dynamics of satellite SSM and the simulated 0–25 cm SM. Across the four RISMA sites, the optimal time differences between the variations of SSM and the 50 cm SM range from 0 to 5 d (0 d for ON2 and ON6, 1 d for ON5, and 5 d for ON4), which is also comparable to the response time difference (about 2 d in the RISMA region) between satellite SSM and the simulated 25–50 cm SM.

The T_{opt} values for SWI estimation based upon the point scale in situ soil moisture measurements at the four RISMA stations are given in Fig. A13. The point-scale T_{opt} values range from 1 to 12 d (1 d for ON2, 2 d for ON6, 3 d for ON4, and 12 d for ON5) for SWI estimation at 20 cm depth, while

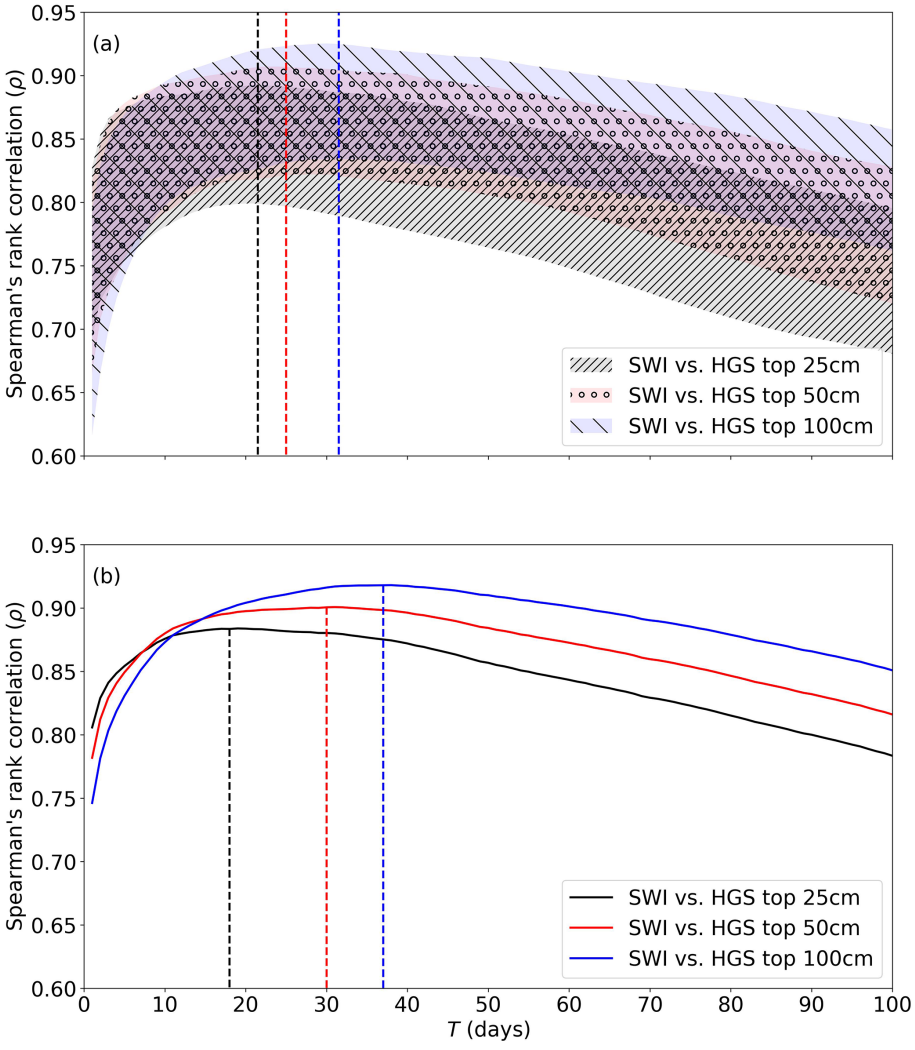

Figure 11. (a) Spearman's rank correlation coefficients between the time series (9 km grid scale) of HGS-simulated SM (from the 0–25, 0–50, and 0–100 cm layers, respectively) and SMAP SSM-derived SWI for the characteristic time length T ranging from 1 to 100 d. For each layer, the shaded band represents the 5th to 95th percentiles of the results from all SMAP grids within the study watershed, with a vertical dashed line indicating the location of the optimal T_{opt} median from all SMAP grids. **(b)** Spearman's rank correlation coefficients between the time series (watershed scale) of HGS-simulated SM (from the 0–25, 0–50, and 0–100 cm layers, respectively) and SMAP SSM-derived SWI for T ranging from 1 to 100 d. For each layer, the vertical dashed line indicates the location of T_{opt} at the watershed scale.

the point-scale T_{opt} values for SWI estimation at 50 cm depth are mostly shorter than 12 d (although the ON4 site shows an T_{opt} of about 50 d for SWI estimation at 50 cm depth, the confidence interval for the T_{opt} is expected to be relatively wide since the highest Spearman's rank correlation varies little over a wide range of T values). Overall, the point-scale T_{opt} values are shorter than those derived from the satellite and model-simulated SM for the 9 km grid scale and the watershed scale. This may indicate that the deeper subsurface layers typically show a quicker response to the near-surface moisture content variability at the point scale.

6.3 Limitations

Numerous modeling studies have demonstrated the influences of tile drains on hydrological behavior in tile-drained agricultural catchments or regions (e.g., De Schepper et al., 2015; Hansen et al., 2013; Que et al., 2015; Rozemeijer et al., 2010; Valayamkunnath et al., 2022). A limitation in the present study is that tile drainage was not explicitly resolved in the HGS model. However, this limitation is unavoidable, due to the extremely complex challenge associated with representing what are effectively a large number of field-scale drainage features in a fully integrated surface water–groundwater model for a $\sim 3900\,km^2$ watershed. While HGS has previously been used to evaluate tile drainage impacts,

the focus has been on much smaller (typically $<50\,km^2$) catchments (e.g., Boico et al., 2022; De Schepper et al., 2015, 2017). To quantify the impact of tile drain omission on the study herein, the fraction of tile drains within each SMAP grid cell is calculated and evaluated in the context of the comparison between SMAP and HGS modeling.

Figure 12 presents scatter plots of tile drain percentage versus calculated performance metrics for the SSM relationship between SMAP and the HGS modeling across all SMAP 9 km cells. The fraction of tile drains shows a statistically significant positive (negative) correlation with the ubRMSD (R and anomaly R). Further, Fig. 13a shows a scatter plot of tile drain percentage versus maximum Spearman's rank correlation between SWI and simulated SM in the 0–100 cm layer, with there being a statistically significant decrease in correlation strength as tile drainage increases. All these results indicate that the lack of tile drainage representation impacted the model performance over the tile drained areas, while also explaining the better agreement between model simulations and SMAP (SSM and SWI) in forested areas than over agricultural fields (Figs. 3, A10b, A10d, and A10f).

However, the tile sensitivity analysis also suggests that the tile drain omission would not negate the findings of the study since it is expected that agreement/linkages between SMAP and HGS modeling would be improved (rather than being discouraged) if tile drainage is explicitly included in the HGS model. Additionally, because the total tile-drained area is only about 25 % of the entire watershed and the fraction of tile drains is less than 30 % for the majority of SMAP grid cells (Fig. 12), the linkages between SMAP and fully integrated surface water–groundwater modeling demonstrated within the results of the study are still representative of the dynamic interplay between near-surface–subsurface water over the study watershed.

The other limitation of the study is that the presence of tile drainage may impact accurate estimation of SWI over the SNW through modifying the percolation process. However, the impact of this limitation is expected to be marginal for this study given the following reasons. Firstly, the fraction of tile drainage is relatively low (<30 %) for most (80 %) of the SMAP 9 km grid cells (Fig. 13). Therefore, the tile drainage would not materially impact the percolation and the SWI estimation for most of the 9 km grids. At the watershed scale, the percentage of total tile-drained area is only about 25 % so that the estimation of watershed-scale SWI should not be significantly influenced either. Secondly, the tile drainage has little impact upon the identified T_{opt}, the only control parameter for the SWI estimation. In this study, T_{opt} was identified by matching the variations in the SWI and simulated subsurface SM. Since the tile drainage was not resolved in the model, the identified T_{opt} and the corresponding SWI estimation was not subject to the presence of tile drainage. Figure 13b provides the scatter plot of the tile drain percentage versus the identified optimal T_{opt} value for the SWI estimation in the 0–100 cm layer. The identified optimal T_{opt} did not exhibit a statistically significant variation with the fraction of tile drainage.

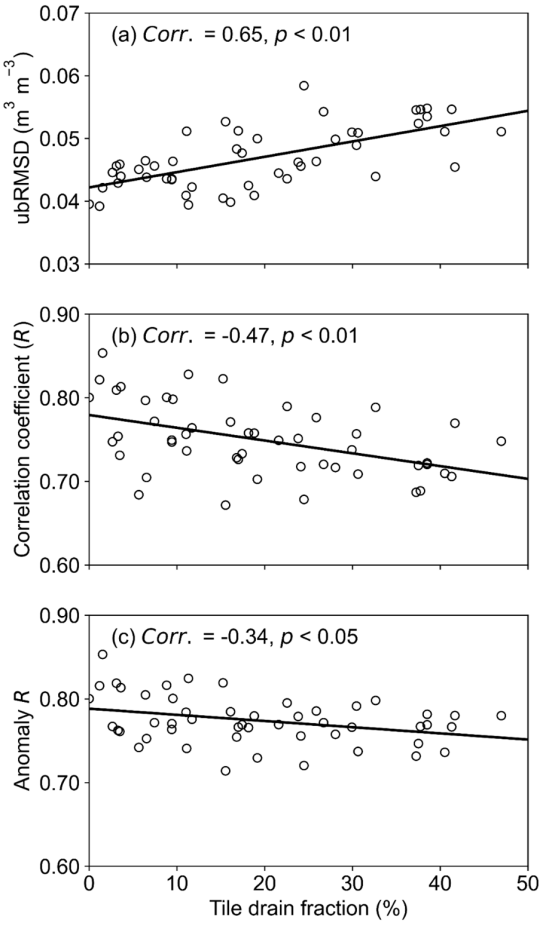

Figure 12. Scatter plot of the percent area of tile drains versus **(a)** ubRMSD, **(b)** R, and **(c)** anomaly R, respectively, across all SMAP grids within the SNW. The calculated performance metrics (shown in Fig. 3) were for HGS-simulated SSM vs SMAP SSM. The Pearson correlation between tile drain fraction and each performance metric, along with the p value, is provided in each plot.

6.4 Other SMAP soil moisture products

In this study, only the SMAP-enhanced L3 radiometer 9 km EASE-Grid SM (SPL3SMP_E) product (O'Neill et al., 2021) was used. The SMAP–Sentinel-1 L2 Radiometer–Radar SM product (Das et al., 2019, 2020), which can provide higher spatial resolution (3 and 1 km) SSM, was not used here because the temporal resolution of the product ($\sim$ 12 d) is not appropriate for detecting the time lags between the variations of SSM and subsurface SM. Further, although the SMAP Level-4 (L4) product can provide the surface (0–5 cm) and root zone (0–100 cm) SM data at 3 h intervals over 9 km EASE-Grid (Reichle et al., 2022), the product is also not suitable for the approaches utilized in this study since the L4 root

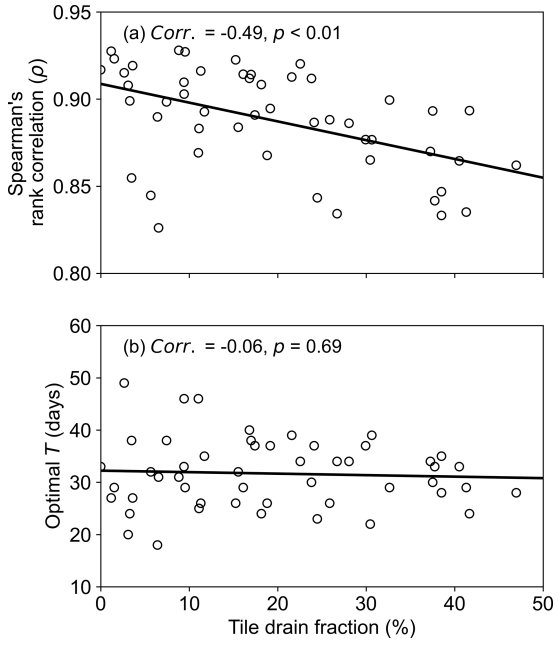

Figure 13. Scatter plot of the percent area of tile drains versus **(a)** the highest Spearman's rank correlation between the SWI series and HGS 0–100 cm SM (as shown in Fig. A10f) and **(b)** the identified optimal T_{opt} value for the root zone layer (as shown in Fig. A10e) across all SMAP grids. In each plot, the Pearson correlation between the two variables, along with the p value, is provided.

zone SM variability is not independent of the SMAP L3/L4 SSM variability. The links between the SMAP SSM and L4 root zone SM variations are controlled by the Catchment land surface model and the assimilation system of SMAP brightness temperatures that were used for producing the L4 product. However, note that the SMAP L4 product is in very good agreement with the HGS model simulations, which were used for representing the subsurface water dynamics in this work, in terms of the root zone SM variability (Fig. A14; the absolute bias between them has no impact on the approaches used in this work, which only considers the temporal variations of SM). This further supports the HGS model's application towards representing the dynamic behavior of subsurface water in this work.

7 Conclusions

The inter-comparison and quantified linkage between the two independent data sources: SMAP measurements (SSM and SWI) and HGS fully integrated surface water–groundwater simulations over a representative agriculture-dominated watershed in eastern Canada led to improved insights into the dynamics of near-surface–subsurface water interaction and the capabilities and approaches of satellite-based SM monitoring and high-resolution fully integrated hydrologic modeling. The SSM variability is a strong reflection of the deeper subsurface water storage fluctuation, and results support the use of SMAP SSM measurements as indicators and/or predictors of root zone SM and shallow GW storage dynamics. Furthermore, the subsurface SM variability can be well represented by SMAP-derived SWI series, which can also be used to predict shallow GW storage change. The vertical coupling strength and the timescale for water traveling from the near-surface to deeper subsurface did not exhibit statistically significant differences across the two spatial scales of investigation, namely SMAP 9 km grid cell and watershed. The high-resolution fully integrated hydrologic simulations conducted with the HGS model performed well in terms of reproducing the variably saturated subsurface water dynamics, although adding the representation of tile drains to the model would further improve the model performance for the tile-drained regions of the subject watershed through the use of remote sensing based SM measurements as validation targets. As satellite SM monitoring continues to evolve, this study has important implications for exploiting the potential of satellite-based SM to predict root zone SM and GW dynamics.

Appendix A

Table A1. Averaged optimal time lags for different soils.

Soils	Soil drainage class	Number of samples	Averaged optimal time lag with the 95 % confidence intervals (in days)			
			0–25 cm SM	25–50 cm SM	50–100 cm SM	GW
Achigan	Imperfectly drained	9	0, [0, 0]	1.00, [0.78, 1.22]	13.0, [11.2, 14.4]	12.3, [11.8, 13.1]
Bainsville	Poorly drained	5	0, [0, 0]	1.20, [1.00, 1.43]	3.6, [3.0, 4.3]	18.8, [14.3, 21.7]
Bearbrook	Poorly drained	10	0, [0, 0]	1.00, [0.82, 1.15]	9.6, [7.5, 11.0]	13.7, [13.5, 14.0]
Brandon	Poorly drained	14	0, [0, 0]	2.21, [1.50, 2.70]	5.9, [5.3, 6.6]	13.6, [13.4, 13.9]
Farmington	Well drained	4	0, [0, 0]	0.75, [0.43, 1.00]	4.5, [4.0, 4.7]	7.5, [6.0, 8.0]
Grenville	Well drained	6	0, [0, 0]	0.67, [0.43, 0.86]	6.0, [5.0, 6.8]	8.7, [7.2, 10.0]

Table A2. Averaged optimal characteristic time length T_{opt} for SWI estimation for different soils.

Soils	Soil drainage class	Number of samples	Averaged T_{opt} with the 95 % confidence intervals (in days).		
			0–25 cm soil layer	0–50 cm soil layer	0–100 cm soil layer
Achigan	Imperfectly drained	9	25, [23, 26]	28, [27, 30]	38, [37, 39]
Bainsville	Poorly drained	5	25, [24, 26]	27, [26, 28]	30, [29, 31]
Bearbrook	Poorly drained	10	21, [20, 22]	24, [23, 24]	32, [31, 33]
Brandon	Poorly drained	14	20, [19, 22]	27, [26, 28]	32, [31, 33]
Farmington	Well drained	4	18, [17, 20]	21, [19, 24]	24, [23, 25]
Grenville	Well drained	6	17, [15, 18]	21, [19, 22]	28, [27, 29]

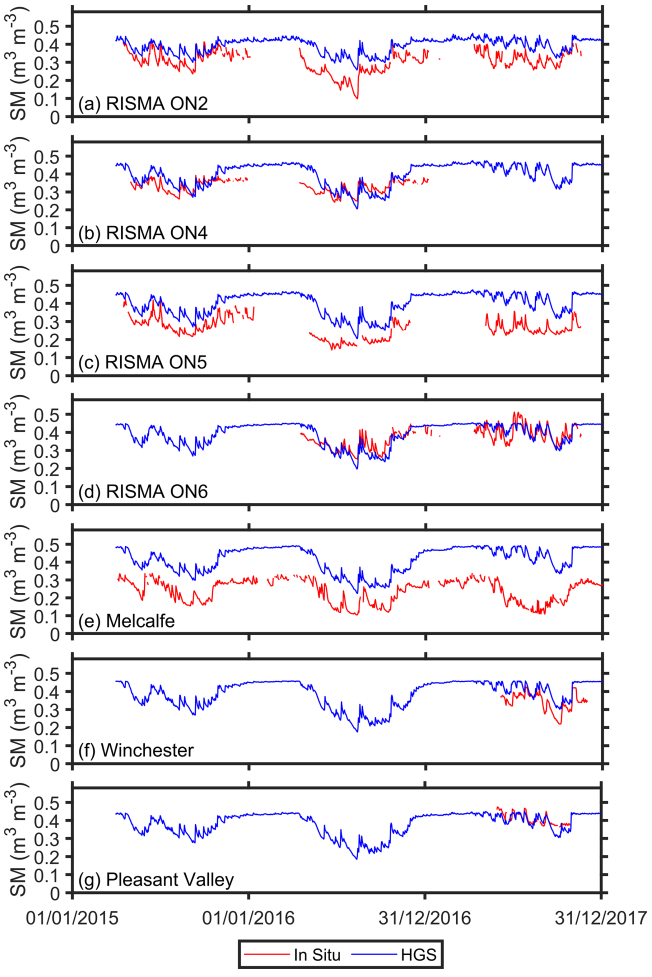

Figure A1. The 0–25 cm depth soil moisture time series of HGS versus in situ at **(a)** ON2, **(b)** ON4, **(c)** ON5, **(d)** ON6, **(e)** Metcalfe, **(f)** Winchester, and **(g)** Pleasant Valley, respectively.

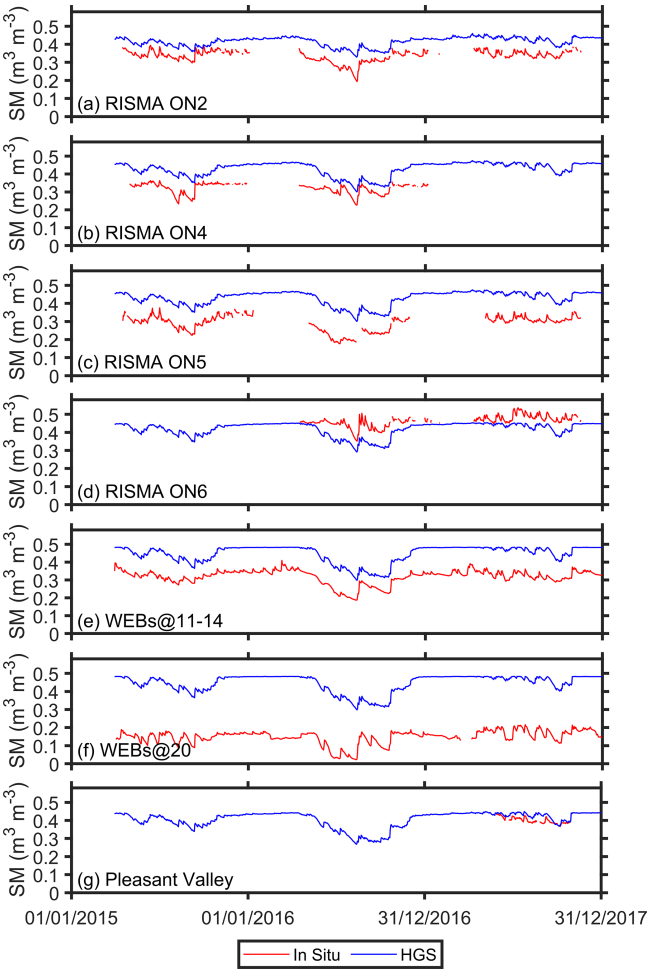

Figure A2. The 0–100 cm depth soil moisture time series of HGS versus in situ at **(a)** ON2, **(b)** ON4, **(c)** ON5, **(d)** ON6, **(e)** WEBs@11–14, **(f)** WEBs@20, and **(g)** Pleasant Valley, respectively.

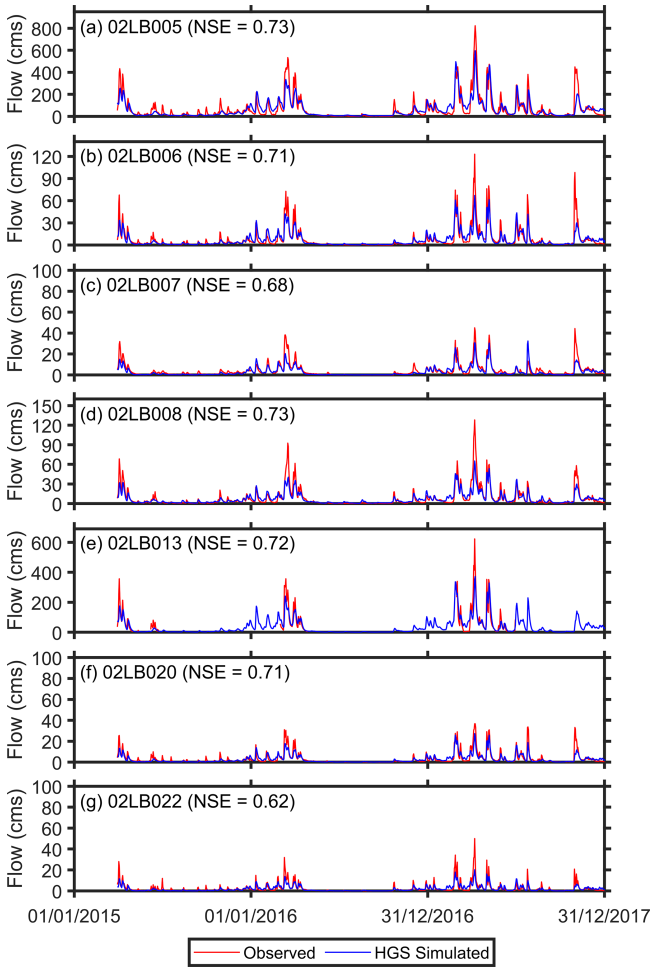

Figure A3. Comparison between the observed and HGS-simulated hydrographs at the seven gauges: **(a)** 02LB005, **(b)** 02LB006, **(c)** 02LB007, **(d)** 02LB008, **(e)** 02LB013, **(f)** 02LB020, and **(g)** 02LB022, respectively. The corresponding Nash–Sutcliffe efficiency (NSE) value is provided in each panel.

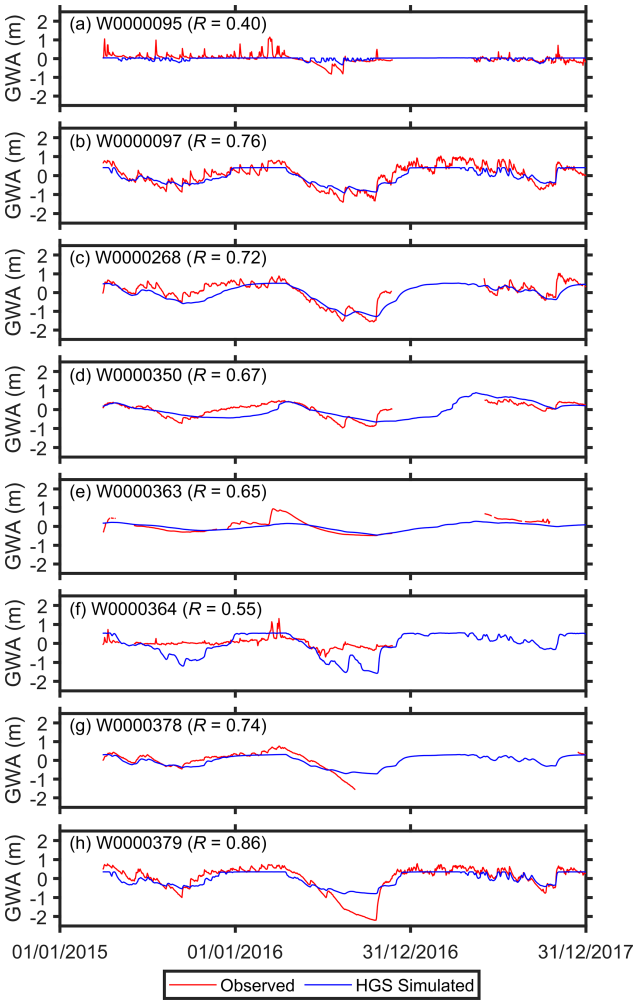

Figure A4. Comparison between the observed and HGS-simulated groundwater level anomalies (GWAs) at the eight GW monitoring wells. The anomalies represent the deviations relative to their respective means over the study period. The corresponding R value is provided in each panel.

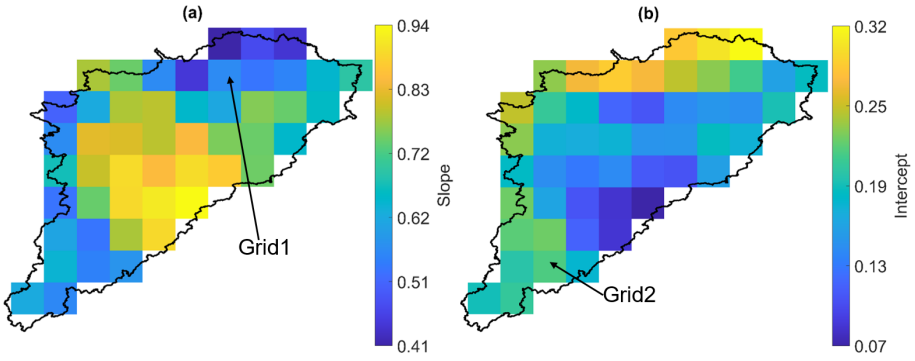

Figure A5. (a) Slope and **(b)** intercept for a linear regression between SMAP SSM (independent variable) and HGS SSM (dependent variable) across all SMAP grids.

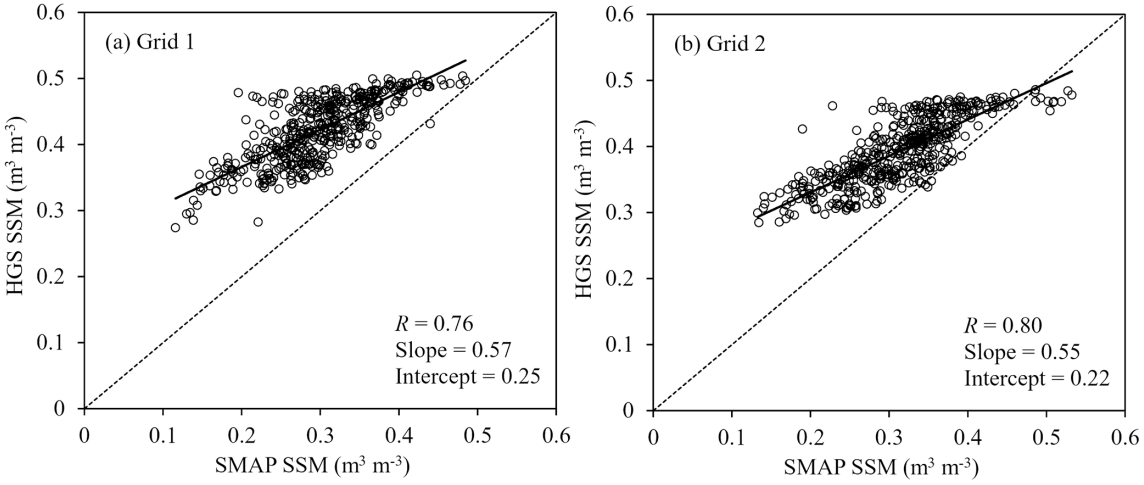

Figure A6. Scatter plots between SMAP SSM and HGS SSM for **(a)** Grid 1 and **(b)** Grid 2, as shown in Fig. A5.

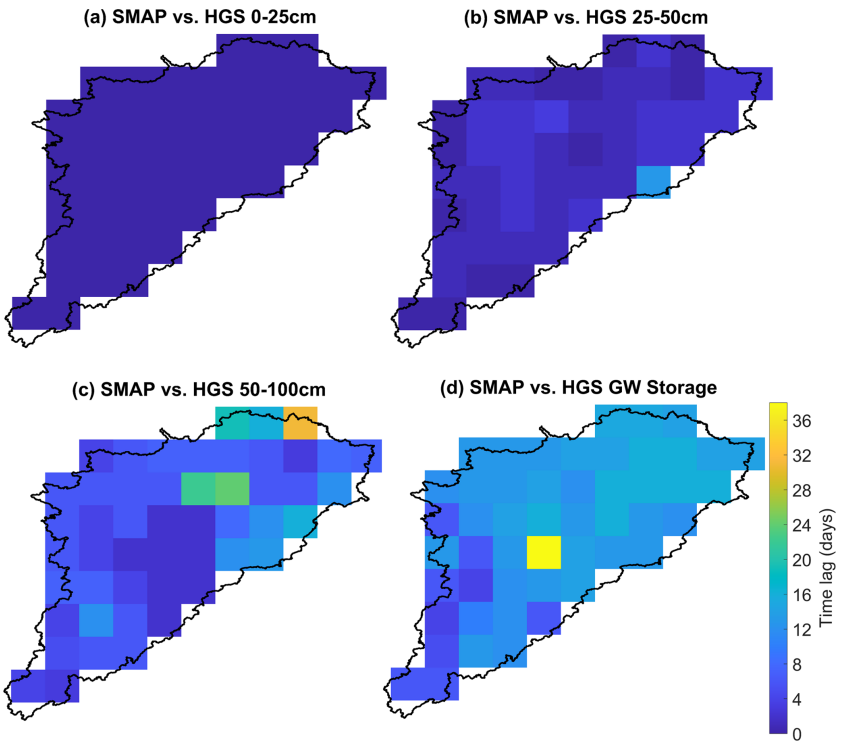

Figure A7. Optimal time lag (in days), relative to the SMAP SSM variability, for HGS-simulated **(a)** 0–25 cm SM, **(b)** 25-50 cm SM, **(c)** 50–100 cm SM, and **(d)** GW storage across all SMAP grids.

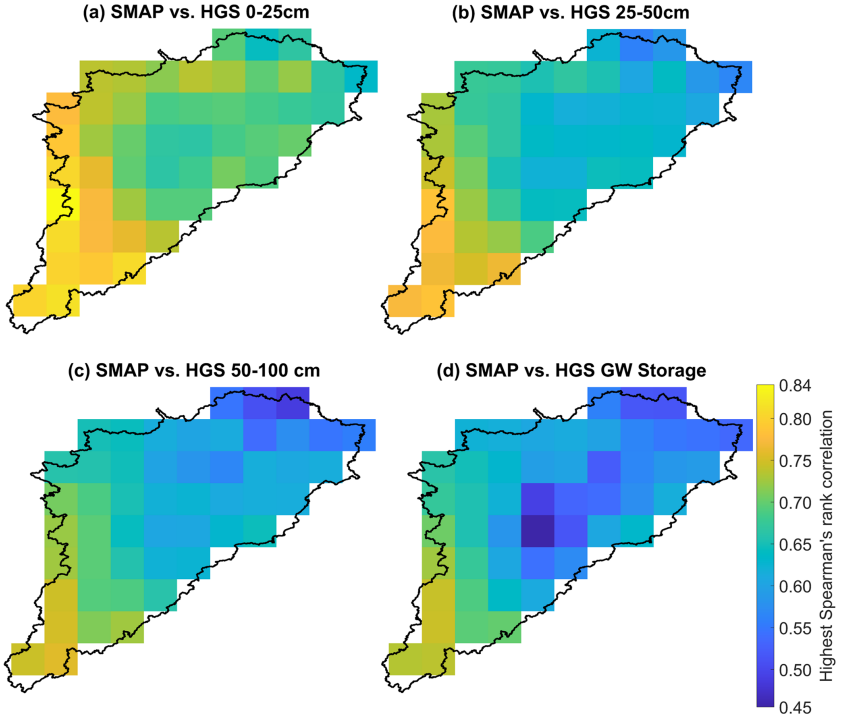

Figure A8. Maximum Spearman's rank correlation between SMAP SSM versus HGS-simulated **(a)** 0–25 cm SM, **(b)** 25–50 cm SM, **(c)** 50–100 cm SM, and **(d)** GW storage, respectively, across all SMAP grids.

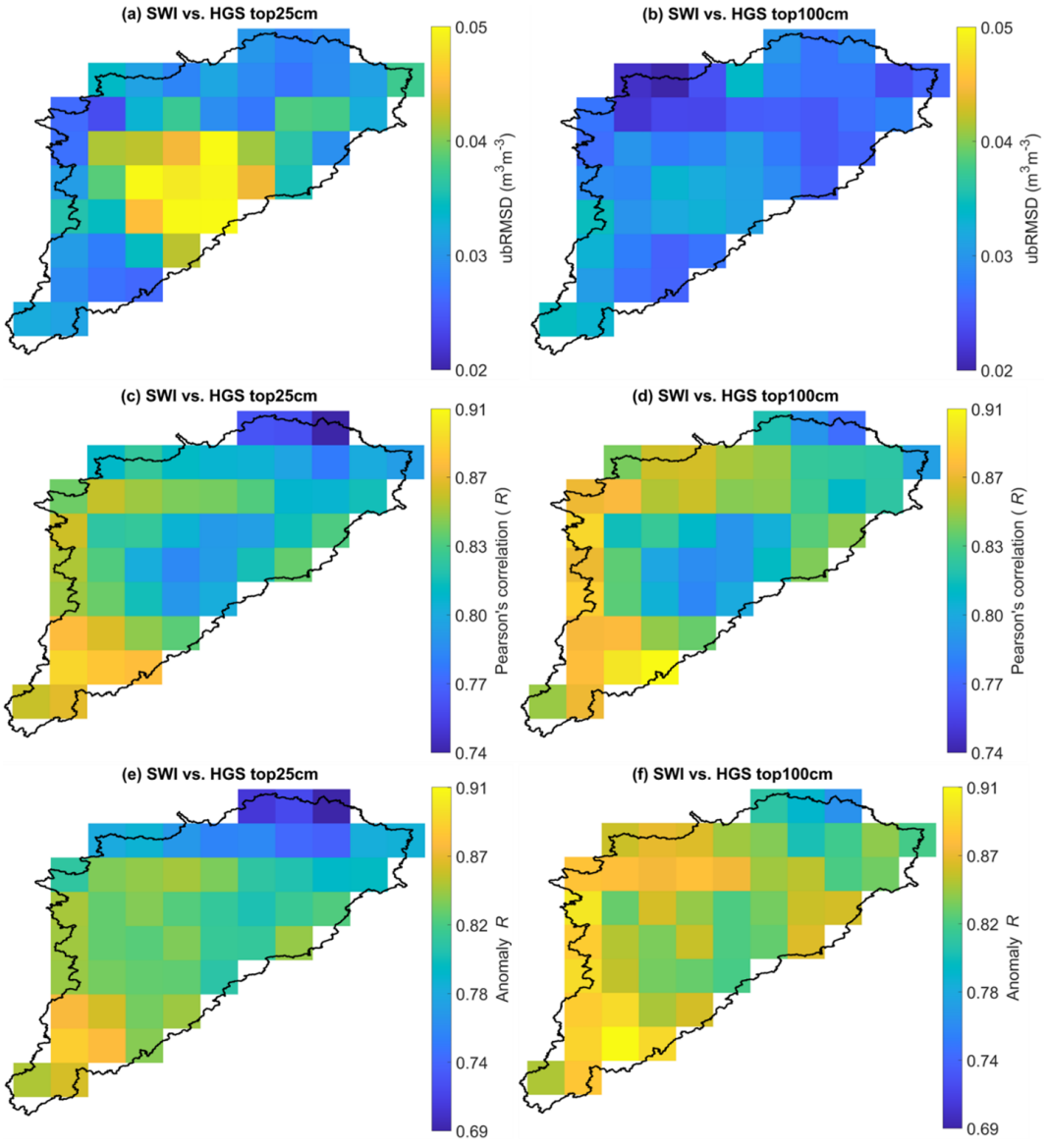

Figure A9. **(a)** ubRMSD, **(c)** R, and **(e)** anomaly R between the SMAP-derived SWI ($T = 15$ d) and HGS-simulated 0–25 cm soil moisture across all SMAP grids over the study watershed. **(b)** ubRMSD, **(d)** R, and **(f)** anomaly R between the SMAP-derived SWI ($T = 20$ d) and HGS-simulated 0–100 cm soil moisture across all SMAP grids over the study watershed.

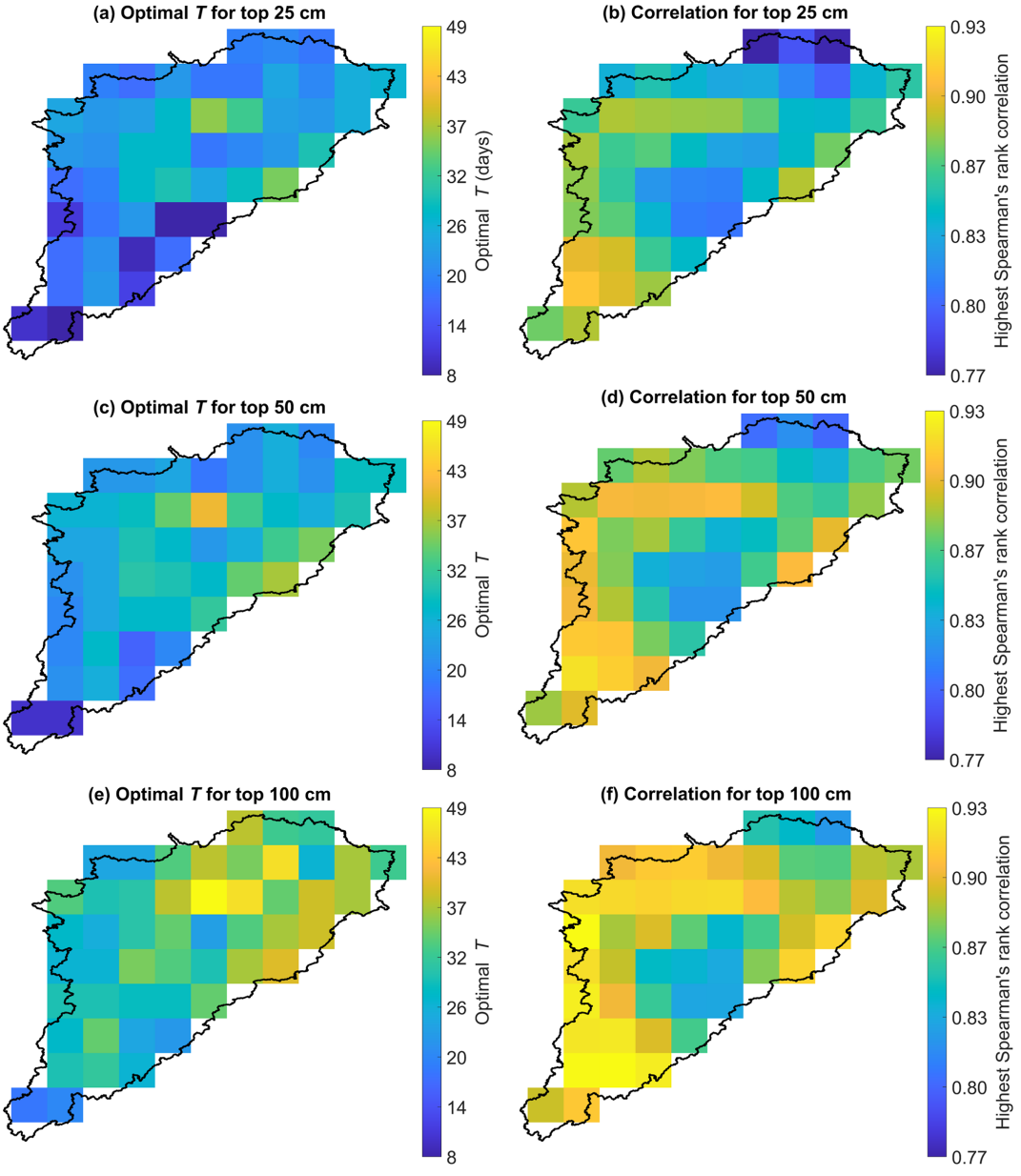

Figure A10. Optimal T_{opt} for SWI estimation for **(a)** 0–25 cm, **(c)** 0–50 cm, and **(e)** 0–100 cm soil layers, respectively. Maximum Spearman's rank correlation between the SWI and simulated soil moisture for **(b)** 0–25 cm, **(d)** 0–50 cm, and **(f)** 0–100 cm soil layers, respectively.

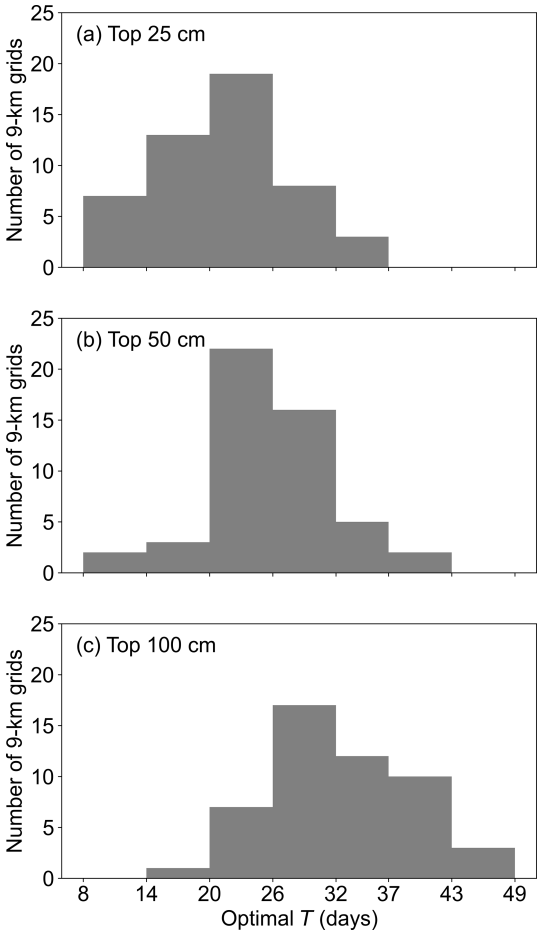

Figure A11. Distribution of the optimal T_{opt} at the 9 km grid scale for **(a)** 0–25 cm, **(b)** 0–50 cm, and **(c)** 0–100 cm soil depths, respectively.

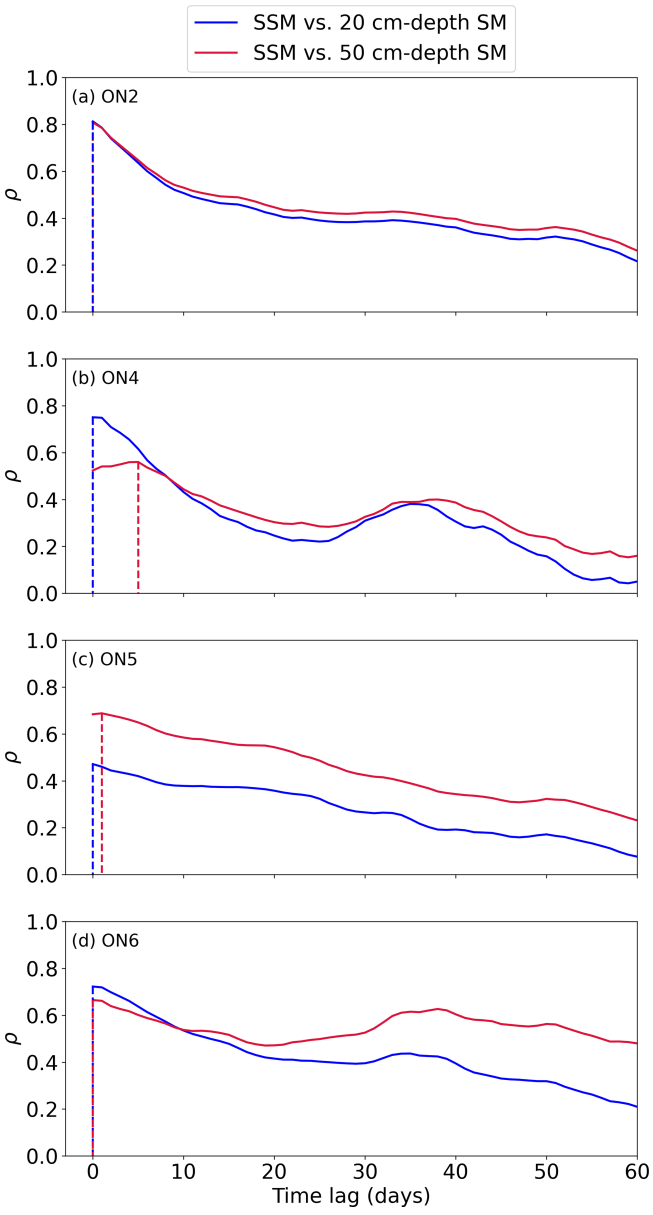

Figure A12. Spearman's rank correlation (ρ) between the near-surface (top 5 cm) soil moisture (SSM) and the subsurface (20 and 50 cm depths) soil moisture (SM) for a time lag ranging from 0 to 60 d based upon the in situ measurements at the four RISMA stations: **(a)** ON2, **(b)** ON4, **(c)** ON5, and **(d)** ON6, respectively. Positive lags indicate that the SSM leads the subsurface SM. The vertical dashed line indicates the optimal time lag corresponding to the maximum ρ between the SSM and subsurface SM.

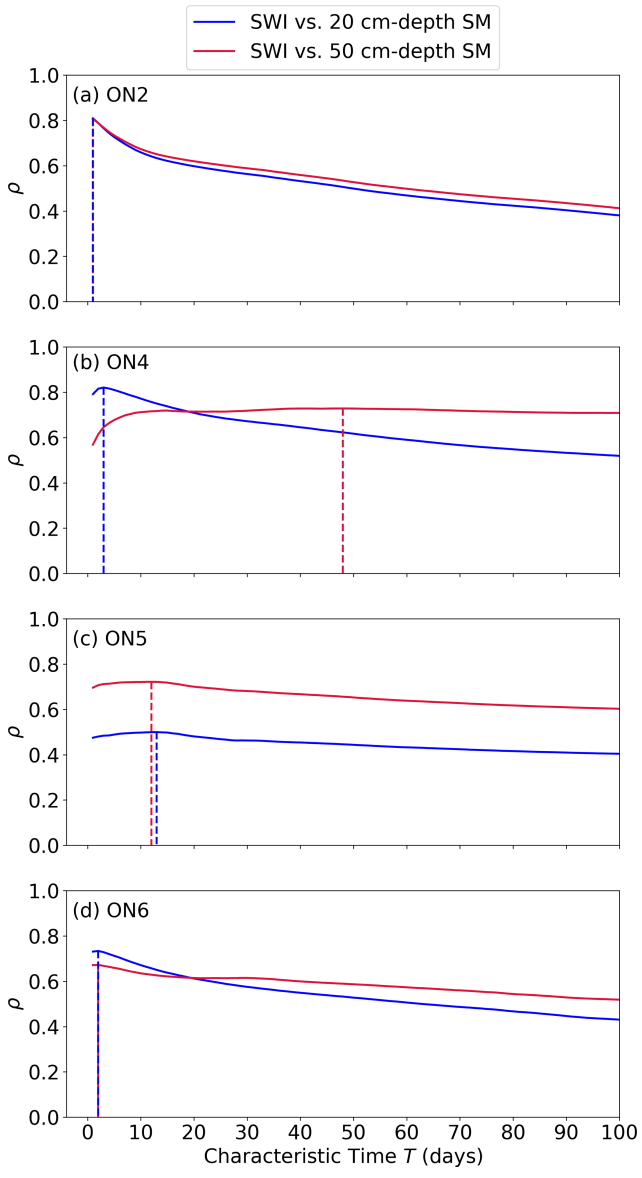

Figure A13. Spearman's rank correlation (ρ) between the subsurface SM (20 and 50 cm depths) and the SSM-derived SWI for the characteristic time T ranging from 1 to 100 d, based upon the in situ measurements at the four RISMA stations: **(a)** ON2, **(b)** ON4, **(c)** ON5, and **(d)** ON6, respectively. The vertical dashed line indicates the location of the optimal characteristic time T_{opt} for SWI estimation.

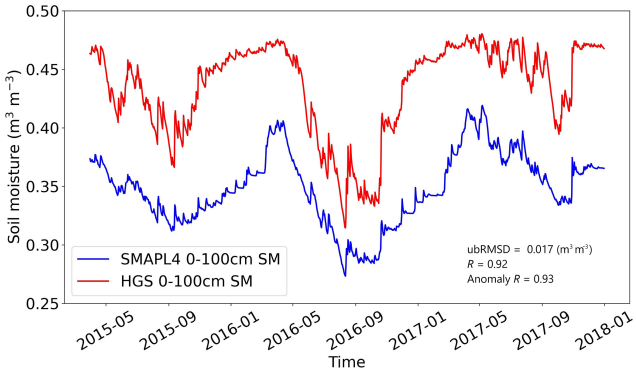

Figure A14. Comparison between the SMAP L4 and HGS simulations for the watershed-averaged root zone (0–100 cm) SM time series. The error metrics (ubRMSD, R, and anomaly R) are calculated without considering the data in winter (December to March), for which satellite SSM measurements are typically not available.

Data availability. The SMAP-enhanced L3 radiometer 9 km EASE-Grid soil moisture (SPL3SMP_E) version 5 product (O'Neill et al., 2021) and the model output from HydroGeoSphere (HGS) (Aquanty, 2022) were used in the creation of this paper. The data are publicly accessible at https://doi.org/10.5281/zenodo.8145252 (Nayak et al., 2023).

Author contributions. AN, XX, and SF conceived the study. AN and XX analyzed the data and wrote the manuscript draft. SF, OK, AE, DL, HR, and ES contributed to the data curation, the analysis, and the editing of the manuscript.

Competing interests. The contact author has declared that none of the authors has any competing interests.

Disclaimer. Publisher's note: Copernicus Publications remains neutral with regard to jurisdictional claims made in the text, published maps, institutional affiliations, or any other geographical representation in this paper. While Copernicus Publications makes every effort to include appropriate place names, the final responsibility lies with the authors.

Acknowledgements. We acknowledge the Canada 1 Water project. Thanks go to the NASA National Snow and Ice Data Center Distributed Active Archive Center for providing access to the SMAP soil moisture product. Thanks also go to the South Nation Conservation Authority for providing the tile drain information.

Financial support. This research has been supported by the Canadian Space Agency (grant no. 21SUESMVAS).

Review statement. This paper was edited by Narendra Das and reviewed by two anonymous referees.

References

Ajami, H., Evans, J. P., McCabe, M. F., and Stisen, S.: Technical Note: Reducing the spin-up time of integrated surface water–groundwater models, Hydrol. Earth Syst. Sci., 18, 5169–5179, https://doi.org/10.5194/hess-18-5169-2014, 2014.

Ajami, H., McCabe, M. F., and Evans, J. P.: Impacts of model initialization on an integrated surface water–groundwater model, Hydro. Process., 29, 3790–3801, https://doi.org/10.1002/hyp.10478, 2015.

Al-Yaari, A., Wigneron, J.-P., Ducharne, A., Kerr, Y. H., Wagner, W., De Lannoy, G., Reichle, R., Al Bitar, A., Dorigo, W., Richaume, P., and Mialon, A.: Global-scale comparison of passive (SMOS) and active (ASCAT) satellite based microwave soil moisture retrievals with soil moisture simulations (MERRA-Land), Remote Sens. Environ., 152, 614–626, https://doi.org/10.1016/j.rse.2014.07.013, 2014.

Albergel, C., Rüdiger, C., Pellarin, T., Calvet, J.-C., Fritz, N., Froissard, F., Suquia, D., Petitpa, A., Piguet, B., and Martin, E.: From near-surface to root-zone soil moisture using an exponential filter: an assessment of the method based on in-situ observations and model simulations, Hydrol. Earth Syst. Sci., 12, 1323–1337, https://doi.org/10.5194/hess-12-1323-2008, 2008.

Aquanty: HydroGeoSphere: A three-dimensional numerical model describing fully integrated subsurface and surface flow and solute transport, Waterloo, ON, https://www.aquanty.com/hgs-download (last access: March 2023), 2022.

Aziz, T., Frey, S. K., Lapen, D. R., Preston, S., Russell, H. A. J., Khader, O., Erler, A. R., and Sudicky, E. A.: Monetizing the role of water in sustaining watershed ecosystem services using a fully integrated subsurface–surface water model, Hydrol. Earth Syst. Sci. Discuss. [preprint], https://doi.org/10.5194/hess-2023-25, in review, 2023.

Bartalis, Z., Wagner, W., Naeimi, V., Hasenauer, S., Scipal, K., Bonekamp, H., Figa, J., and Anderson, C.: Initial soil moisture retrievals from the METOP-A Advanced Scatterometer (ASCAT), Geophys. Res. Lett., 34, L20401. https://doi.org/10.1029/2007GL031088, 2007.

Boico, V.F., Therrien, R., Delottier, H., Young, N. L., and Højberg, A.L.: Comparing alternative conceptual models for tile drains and soil heterogeneity for the simulation of tile drainage in agricultural catchments, J. Hydrol., 612, 128120, https://doi.org/10.1016/j.jhydrol.2022.128120, 2022.

Bouaziz, L. J. E., Steele-Dunne, S. C., Schellekens, J., Weerts, A. H., Stam, J., Sprokkereef, E.,Winsemius, H. H. C., Savenije, H. H. C., and Hrachowitz, M.: Improved Understanding of the Link Between Catchment-Scale Vegetation Accessible Storage and Satellite-Derived Soil Water Index, Water Resour. Res., 56, e2019WR026365, https://doi.org/10.1029/2019WR026365, 2020.

Ceballos, A., Scipal, K., Wagner, W., and Martínez-Fernández, J.: Validation of ERS scatterometer-derived soil moisture data in the central part of the Duero Basin, Spain, Hydro. Process., 19, 1549–1566, https://doi.org/10.1002/hyp.5585, 2005.

Colliander, A., Jackson, T. J., Bindlish, R., Chan, S., Das, N., Kim, S. B., Cosh, M. H., Dunbar, R. S., Dang, L., Pashaian, L., Asanuma, J., Aida, K., Berg, A., Rowlandson, T., Bosch, D., Caldwell, T., Caylor, K., Goodrich, D., al Jassar, H., Lopez-Baeza, E., Martínez-Fernández, J., González-Zamora, A., Livingston, S., McNairn, H., Pacheco, A., Moghaddam, M., Montzka, C., Notarnicola, C., Niedrist, G., Pellarin, T., Prueger, J., Pulliainen, J., Rautiainen, K., Ramos, J., Seyfried, M., Starks, P., Su, Z., Zeng, Y., van der Velde, R., Thibeault, M., Dorigo, W., Vreugdenhil, M., Walker, J. P., Wu, X., Monerris, A., O'Neill, P. E., Entekhabi, D., Njoku, E. G., and Yueh, S.: Validation of SMAP surface soil moisture products with core validation sites, Remote Sens. Environ., 191, 215–231, https://doi.org/10.1016/j.rse.2017.01.021, 2017.

de Lange, R., Beck, R., van de Giesen, N., Friesen, J., de Wit, A., and Wagner, W.: Scatterometer-derived soil moisture calibrated for soil texture with a one-dimensional water-flow model, IEEE T. Geosci. Remote, 46, 4041–4049, https://doi.org/10.1109/TGRS.2008.2000796, 2008.

De Schepper, G., Therrien, R., Refsgaard, J. C., and Hansen, A. L.: Simulating coupled surface and subsurface water flow in a tile-drained agricultural catchment, J. Hydrol., 521, 374–388, https://doi.org/10.1016/j.jhydrol.2014.12.035, 2015.

De Schepper, G., Therrien, R., Refsgaard, J. C., He, X., Kjaergaard, C., and Iversen, B. V.: Simulating seasonal variations of tile drainage discharge in an agricultural catchment, Water Resour. Res., 53, 3896–3920, https://doi.org/10.1002/2016WR020209, 2017.

Das, N., Entekhabi, D., Dunbar, R. S., Chaubell, M. J., Colliander, A., Yueh, S., Jagdhuber, T., Chen, F., Crow, W. T., O'Neill, P. E., Walker, J. P., Berg, A., Bosch, D. D., Caldwell, T., Cosh, M. H., Collins, C. H., Lopez-Baeza, E., and Thibeault, M.: The SMAP and Copernicus Sentinel 1A/B microwave active-passive high resolution surface soil moisture product, Remote Sens. Environ., 233, 111380, https://doi.org/10.1016/j.rse.2019.111380, 2019.

Das, N., Entekhabi, D., Dunbar, R. S., Kim, S., Yueh, S., Colliander, A., O'Neill, P. E., Jackson, T., Jagdhuber, T., Chen, F., Crow, W. T., Walker, J., Berg, A., Bosch, D., Caldwell, T., and Cosh, M.: SMAP/Sentinel-1 L2 Radiometer/Radar 30-Second Scene 3 km EASE-Grid Soil Moisture, Version 3, NASA National Snow and Ice Data Center Distributed Active Archive Center Boulder, CO, USA, https://doi.org/10.5067/ASB0EQO2LYJV, 2020.

Dobriyal, P., Qureshi, A., Badola, R., and Hussain, S. A.: A review of the methods available for estimating soil moisture and its implications for water resource management, J. Hydrol., 458–459, 110–117, https://doi.org/10.1016/j.jhydrol.2012.06.021, 2012.

Dorigo, W. A., Scipal, K., Parinussa, R. M., Liu, Y. Y., Wagner, W., de Jeu, R. A. M., and Naeimi, V.: Error characterisation of global active and passive microwave soil moisture datasets, Hydrol. Earth Syst. Sci., 14, 2605–2616, https://doi.org/10.5194/hess-14-2605-2010, 2010.

Draper, C., Reichle, R., de Jeu, R., Naeimi, V., Parinussa, R., and Wagner, W.: Estimating root mean square errors in remotely sensed soil moisture over continental scale domains, Remote Sens. Environ., 137, 288–298, https://doi.org/10.1016/j.rse.2013.06.013, 2013.

Entekhabi, D., Njoku, E. G., O'Neill, P. E., Kellogg, K. H., Crow, W. T., Edelstein, W. N., Entin, J. K., Goodman, S. D., Jackson, T. J., Johnson, J., Kimball, J., Piepmeier, J. R.,

Koster, R. D., Martin, N., McDonald, K. C., Moghaddam, M., Moran, S., Reichle, R., Shi, J. C., Spencer, M. W., Thurman, S. W., Tsang, L., and Van Zyl, J.: The Soil Moisture Active Passive (SMAP) mission, P. IEEE, 98, 704–716, https://doi.org/10.1109/JPROC.2010.2043918, 2010.

Erdal, D., Baroni, G., Sánchez-León, E., and Cirpka, O. A.: The value of simplified models for spin up of complex models with an application to subsurface hydrology, Comput. Geosci., 126, 62–72, https://doi.org/10.1016/j.cageo.2019.01.014, 2019.

Erler, A. R., Frey, S. K., Khader, O., d'Orgeville, M., Park, Y., Hwang, H., Lapen, D. R., Peltier, W. R., and Sudicky, E. A.: Evaluating climate change impacts on soil moisture and groundwater resources within a lake-affected region, Water Resour. Res., 55, 8142–8163, https://doi.org/10.1029/2018WR023822, 2019.

Famiglietti, J. S., Lo, M., Ho, S. L., Bethune, J., Anderson, K. J., Syed, T. H., Swenson, S. C., de Linage, C. R., and Rodell, M.: Satellites measure recent rates of groundwater depletion in California's Central Valley, Geophys. Res. Lett., 38, 2010GL046442. https://doi.org/10.1029/2010GL046442, 2011.

Ford, T. W., Harris, E., and Quiring, S. M.: Estimating root zone soil moisture using near-surface observations from SMOS, Hydrol. Earth Syst. Sci., 18, 139–154, https://doi.org/10.5194/hess-18-139-2014, 2014.

Frey, S. K., Miller, K., Khader, O., Taylor, A., Morrison, D., Xu, X., Berg, S. J., Hwang, H. T., Sudicky, E. A., and Lapen, D. R.: Evaluating landscape influences on hydrologic behavior with a fully-integrated groundwater – surface water model, J. Hydrol., 602, 126758, https://doi.org/10.1016/j.jhydrol.2021.126758, 2021.

Hansen, A. L., Refsgaard, J. C., Christensen, B. S. B., and Jensen, K. H.: Importance of including small-scale tile drain discharge in the calibration of a coupled groundwater-surface water catchment model, Water Resour. Res., 49, 585–603, https://doi.org/10.1029/2011WR011783, 2013.

Hwang, H. T., Park, Y. J., Sudicky, E., and Forsyth, P. A.: A parallel computational framework to solve flow and transport in integrated surface–subsurface hydrologic systems, Environ. Modell. Softw., 61, 39–58, https://doi.org/10.1016/j.envsoft.2014.06.024, 2014.

Jonard, F., Bogena, H., Caterina, D., Garré, S., Klotzsche, A., Monerris, A., Schwank, M., and von Hebel, C.: Ground-based soil moisture determination, in: Observation and Measurement of Ecohydrological Processes, 1–42, Springer, Berlin, Heidelberg, https://doi.org/10.1007/978-3-662-47871-4_2-1, 2018.

Kerr, Y. H., Waldteufel, P., Wigneron, J.-P., Delwart, S., Cabot, F., Boutin, J., Escorihuela, M.-J., Font, J., Reul, N., Gruhier, C., Juglea, S., Drinkwater, M., Hahne, A., Martin-Neira, M., and Mecklenburg, S.: The SMOS mission: New tool for monitoring key elements of the global water cycle, P. IEEE, 98, 666–687, https://doi.org/10.1109/JPROC.2010.2043032, 2010.

Logan, C., Cummings, D. I., Pullan, S., Pugin, A., Russell, H. A. J., and Sharpe, D. R.: Hydrostratigraphic model of the South Nation watershed region, south-eastern Ontario, Geological Survey of Canada, 17 pp., https://doi.org/10.4095/248203, 2009.

Mahmood, R. and Hubbard, K. G.: Relationship between soil moisture of near surface and multiple depths of the root zone under heterogeneous land uses and varying hydroclimatic conditions, Hydrol. Process., 21, 3449–3462, https://doi.org/10.1002/hyp.6578, 2007.

Mahmood, R., Littell, A., Hubbard, K. G., and You, J.: Observed data-based assessment of relationships among soil moisture at various depths, precipitation, and temperature, Appl. Geogr., 34, 255–264, https://doi.org/10.1016/j.apgeog.2011.11.009, 2012.

Manfreda, S., Brocca, L., Moramarco, T., Melone, F., and Sheffield, J.: A physically based approach for the estimation of root-zone soil moisture from surface measurements, Hydrol. Earth Syst. Sci., 18, 1199–1212, https://doi.org/10.5194/hess-18-1199-2014, 2014.

McKenney, D. W., Hutchinson, M. F., Papadopol, P., Lawrence, K., Pedlar, J., Campbell, K., Milewska, E., Hopkinson, R. F., Price, D., and Owen, T.: Customized spatial climate models for North America, B. Am. Meteorol. Soc., 92, 1611–1622, https://doi.org/10.1175/2011bams3132.1, 2011.

Muñoz-Sabater, J., Dutra, E., Agustí-Panareda, A., Albergel, C., Arduini, G., Balsamo, G., Boussetta, S., Choulga, M., Harrigan, S., Hersbach, H., Martens, B., Miralles, D. G., Piles, M., Rodríguez-Fernández, N. J., Zsoter, E., Buontempo, C., and Thépaut, J.-N.: ERA5-Land: a state-of-the-art global reanalysis dataset for land applications, Earth Syst. Sci. Data, 13, 4349–4383, https://doi.org/10.5194/essd-13-4349-2021, 2021.

Nayak, A. K., Biswal, B., and Sudheer, K. P.: A novel framework to determine the usefulness of satellite-based soil moisture data in streamflow prediction using dynamic Budyko model, J. Hydrol., 595, 125849, https://doi.org/10.1016/j.jhydrol.2020.125849, 2021.

Nayak, A. K., Xu, X., Frey, S. K., Khader, O., Erler, A. R., Lapen, D. R., Russell, H. A. J., and Sudicky, E. A.: Quantifying the linkage between SMAP soil moisture and fully-integrated hydrologic simulations, Zenodo [data set], https://doi.org/10.5281/zenodo.8145252, 2023.

Njoku, E. G., Jackson, T. J., Lakshmi, V., Chan, T. K., and Nghiem, S. V.: Soil moisture retrieval from AMSR-E, IEEE T. Geosci. Remote Sens., 41, 215–228, https://doi.org/10.1109/TGRS.2002.808243, 2003.

O'Neill, P. E., Chan, S., Njoku, E. G., Jackson, T., Bindlish, R., Chaubell, J., and Colliander, A.: SMAP enhanced L3 radiometer global and polar grid daily 9 km EASE-grid soil moisture, version 5, NASA National Snow and Ice Data Center Distributed Active Archive Center, Boulder, CO, USA, https://doi.org/10.5067/4DQ54OUIJ9DL, 2021.

Owe, M., de Jeu, R., and Holmes, T.: Multisensor historical climatology of satellite-derived global land surface moisture, J. Geophys. Res., 113, F01002, https://doi.org/10.1029/2007JF000769, 2008.

Reichle, R. H., De Lannoy, G., Koster, R. D., Crow, W. T., Kimball, J. S., Liu, Q., and Bechtold, M.: SMAP L4 Global 3-hourly 9 km EASE-Grid Surface and Root Zone Soil Moisture Analysis Update, Version 7, NASA National Snow and Ice Data Center Distributed Active Archive Center, Boulder, Colorado, USA, https://doi.org/10.5067/LWJ6TF5SZRG3, 2022.

Parrens, M., Zakharova, E., Lafont, S., Calvet, J.-C., Kerr, Y., Wagner, W., and Wigneron, J.-P.: Comparing soil moisture retrievals from SMOS and ASCAT over France, Hydrol. Earth Syst. Sci., 16, 423–440, https://doi.org/10.5194/hess-16-423-2012, 2012.

Paulik, C., Dorigo, W., Wagner, W., and Kidd, R.: Validation of the ASCAT Soil Water Index using in situ data from the International Soil moisture network. Int. J. Appl. Earth Obs., 30, 1–8, https://doi.org/10.1016/j.jag.2014.01.007, 2014.

Que, Z., Seidou, O., Droste, R. L., Wilkes, G., Sunohara, M., Topp, E., and Lapen, D. R.: Using AnnAGNPS to predict the effects of tile drainage control on nutrient and sediment loads for a river basin, J. Environ. Qual., 44, 629–641, https://doi.org/10.2134/jeq2014.06.0246, 2015.

Ragab, R.: Towards a continuous operational system to estimate the root-zone soil moisture from intermittent remotely sensed surface moisture, J. Hydrol., 173, 1–25, https://doi.org/10.1016/0022-1694(95)02749-F, 1995.

Rodell, M., Chen, J., Kato, H., Famiglietti, J. S., Nigro, J., and Wilson, C. R.: Estimating groundwater storage changes in the Mississippi River basin (USA) using GRACE, Hydrogeol. J., 15, 159–166, https://doi.org/10.1007/s10040-006-0103-7, 2007.

Rodell, M., Velicogna, I., and Famiglietti, J. S.: Satellite-based estimates of groundwater depletion in India, Nature, 460, 999–1002, 2009.

Rodell, M., Famiglietti, J. S., and Wiese, D. N.: Emerging trends in global freshwater availability, Nature, 557, 651–659, https://doi.org/10.1038/s41586-018-0123-1, 2018.

Rozemeijer, J. C., van der Velde, Y., McLaren, R. G., van Geer, F. C., Broers, H. P., and Bierkens, M. F. P.: Integrated modeling of groundwater-surface water interactions in a tile-drained agricultural field: The importance of directly measured flow route contributions, Water Resour. Res., 46, W11537, https://doi.org/10.1029/2010WR009155, 2010.

Simmons, C. T., Brunner, P., Therrien, R., and Sudicky, E. A.: Commemorating the 50th anniversary of the Freeze and Harlan (1969) Blueprint for a physically-based, digitally-simulated hydrologic response model, J. Hydrol., 584, 124309, https://doi.org/10.1016/j.jhydrol.2019.124309, 2020.

Singh, G., Panda, R. K., and Mohanty, B. P.: Spatiotemporal Analysis of Soil Moisture and Optimal Sampling Design for Regional-Scale Soil Moisture Estimation in a Tropical Watershed of India, Water Resour. Res., 55, 2057–2078, https://doi.org/10.1029/2018WR024044, 2019.

Sunohara, M. D., Gottschall, N., Wilkes, G., Craiovan, E., Topp, E., Que, Z., Seidou, O., Frey, S. K., and Lapen, D. R.: Long-term observations of nitrogen and phosphorus export in paired-agricultural watersheds under controlled and conventional tile drainage, J. Environ. Qual., 44, 1589–1604, https://doi.org/10.2134/jeq2015.01.0008, 2015.

Sutanudjaja, E. H., de Jong, S. M., van Geer, F. C., and Bierkens, M. F. P.: Using ERS spaceborne microwave soil moisture observations to predict groundwater head in space and time, Remote Sens. Environ., 138, 172–188, https://doi.org/10.1016/j.rse.2013.07.022, 2013.

Syed, T. H., Famiglietti, J. S., Rodell, M., Chen, J., and Wilson, C. R.: Analysis of terrestrial water storage changes from GRACE and GLDAS, Water Resour. Res., 44, W02433, https://doi.org/10.1029/2006WR005779, 2008.

Tapley, B. D., Bettadpur, S., Ries, J. C., Thompson, P. F., and Watkins, M. M.: GRACE measurements of mass variability in the earth system, Science, 305, 503–505, https://doi.org/10.1126/science.1099192, 2004.

Tian, J., Han, Z., Bogena, H. R., Huisman, J. A., Montzka, C., Zhang, B., and He, C.: Estimation of subsurface soil moisture from surface soil moisture in cold mountainous areas, Hydrol. Earth Syst. Sci., 24, 4659–4674, https://doi.org/10.5194/hess-24-4659-2020, 2020.

Thomas, B. F. and Famiglietti, J. S.: Identifying climate-induced groundwater depletion in GRACE observations, Sci. Rep., 9, 4124, https://doi.org/10.1038/s41598-019-40155-y, 2019.

Valayamkunnath, P., Gochis, D. J., Chen, F., Barlage, M., and Franz, K. J.: Modeling the hydrologic influence of subsurface tile drainage using the National Water Model, Water Resour. Res., 58, e2021WR031242, https://doi.org/10.1029/2021WR031242, 2022.

Wagner, W., Lemoine, G., and Rott, H.: A method for estimating soil moisture from ERS Scatterometer and soil data, Remote Sens. Environ., 70, 191–207, https://doi.org/10.1016/S0034-4257(99)00036-X, 1999.

Wang, T., Franz, T. E., You, J., Shulski, M. D., and Ray, C.: Evaluating controls of soil properties and climatic conditions on the use of an exponential filter for converting near surface to root zone soil moisture contents, J. Hydrol., 548, 683–696, https://doi.org/10.1016/j.jhydrol.2017.03.055, 2017.

Wu, W., Geller, M. A., and Dickinson, R. E.: The response of soil moisture to long-term variability of precipitation, J. Hydrometeorol., 3, 604–613, https://doi.org/10.1175/1525-7541(2002)003<0604:TROSMT>2.0.CO;2, 2002.

Xu, S., Frey, S. K., Erler, A. R., Khader, O., Berg, S. J., Hwang, H. T., Callaghan, M. V., Davison, J. H., and Sudicky, E. A.: Investigating groundwater-lake interactions in the Laurentian Great Lakes with a fully-integrated surface water-groundwater model, J. Hydrol., 594, 125911, https://doi.org/10.1016/j.jhydrol.2020.125911, 2021.

Xu, X., Li, J., and Tolson, B. A.: Progress in integrating remote sensing data and hydrologic modeling, Prog. Phys. Geogr., 38, 464–498, https://doi.org/10.1177/0309133314536583, 2014.

Xu, X.: Evaluation of SMAP level 2, 3, and 4 soil moisture datasets over the Great Lakes region, Remote Sens., 12, 3785, https://doi.org/10.3390/rs12223785, 2020.

Xu, X. and Frey, S.K.: Validation of SMOS, SMAP, and ESA CCI soil moisture over a humid region, IEEE J. Sel. Top. Appl., 14, 10784–10793, https://doi.org/10.1109/JSTARS.2021.3122068, 2021.

Zhang, N., Quiring, S., Ochsner, T., and Ford, T.: Comparison of three methods for vertical extrapolation of soil moisture in Oklahoma, Vadose Zone J., 16, vzj2017.04.0085, https://doi.org/10.2136/vzj2017.04.0085, 2017.

Zhao, D., Kuenzer, C., Fu, C., and Wagner, W.: Evaluation of the ERS Scatterometer-Derived Soil Water Index to Monitor Water Availability and Precipitation Distribution at Three Different Scales in China, J. Hydrometeorol., 9, 549–562, https://doi.org/10.1175/2007JHM965.1, 2008.

Zhu, Y., Myint, S. W., Schaffer-Smith, D., Sauchyn, D. J., Xu, X., Piwowar, J. M., and Li, Y.: Examining ground and surface water changes in response to environmental variables, land use dynamics, and socioeconomic changes in Canada, J. Environ. Manage., 322, 115875, https://doi.org/10.1016/j.jenvman.2022.115875, 2022.